Battery-free, lightweight, injectable microsystem for in vivo wireless pharmacology and optogenetics

Yi Zhang[a,b,1], Daniel C. Castro[c,1], Yuan Han[d,e,f], Yixin Wu[b], Hexia Guo[b], Zhengyan Weng[a], Yeguang Xue[b,g,h], Jokubas Ausra[i], Xueju Wang[j], Rui Li[k,l], Guangfu Wu[a], Abraham Vázquez-Guardado[m], Yiwen Xie[b], Zhaoqian Xie[g,h,k], Diana Ostojich[b], Dongsheng Peng[n], Rujie Sun[o], Binbin Wang[p], Yongjoon Yu[q], John P. Leshock[b], Subing Qu[r], Chun-Ju Su[b], Wen Shen[s], Tao Hang[t], Anthony Banks[b], Yonggang Huang[b,g,h,m], Jelena Radulovic[d], Philipp Gutruf[i,2], Michael R. Bruchas[c,u,v,2], and John A. Rogers[b,m,w,x,y,z,2]

[a]Department of Biomedical, Biological, and Chemical Engineering, University of Missouri, Columbia, MO 65211; [b]Department of Materials Science and Engineering, Northwestern University, Evanston, IL 60208; [c]Department of Anesthesiology and Pain Medicine, University of Washington, Seattle, WA 98195; [d]Department of Psychiatry and Behavioral Sciences, Northwestern University, Chicago, IL 60611; [e]Department of Anesthesiology, Eye & ENT Hospital, Fudan University, 200031 Shanghai, China; [f]Jiangsu Province Key Laboratory of Anesthesiology, Xuzhou Medical University, 221004 Xuzhou, China; [g]Department of Civil and Environmental Engineering, Northwestern University, Evanston, IL 60208; [h]Department of Mechanical Engineering, Northwestern University, Evanston, IL 60208; [i]Biomedical Engineering, College of Engineering, The University of Arizona, Tucson, AZ 85721; [j]Department of Mechanical and Aerospace Engineering, University of Missouri, Columbia, MO 65211; [k]State Key Laboratory of Structural Analysis for Industrial Equipment, Department of Engineering Mechanics, Dalian University of Technology, 116024 Dalian, China; [l]International Research Center for Computational Mechanics, Dalian University of Technology, 116024 Dalian, China; [m]Center for Bio-Integrated Electronics, Northwestern University, Evanston, IL 60208; [n]College of Optoelectronic Engineering, Shenzhen University, 518060 Shenzhen, China; [o]Bristol Composites Institute, University of Bristol, BS8 1TR Bristol, United Kingdom; [p]Department of Civil and Environmental Engineering, University of Missouri, Columbia, MO 65211; [q]NeuroLux, Inc., Evanston, IL 60201; [r]Department of Materials Science and Engineering, Materials Research Laboratory, University of Illinois at Urbana–Champaign, Urbana, IL 61801; [s]Department of Mechanical and Aerospace Engineering, University of Texas at Arlington, Arlington, TX 76019; [t]School of Materials Science and Engineering, Shanghai Jiao Tong University, 200240 Shanghai, China; [u]Center for Neurobiology of Addiction, Pain, and Emotion, University of Washington, Seattle, WA 98195; [v]Department of Pharmacology, University of Washington, Seattle, WA 98195; [w]Simpson Querrey Institute, Northwestern University, Chicago, IL 60611; [x]Department of Biomedical Engineering, Northwestern University, Evanston, IL 60208; [y]Department of Chemistry, Northwestern University, Evanston, IL 60208; and [z]Department of Neurological Surgery, Feinberg School of Medicine, Northwestern University, Chicago, IL 60611

Pharmacology and optogenetics are widely used in neuroscience research to study the central and peripheral nervous systems. While both approaches allow for sophisticated studies of neural circuitry, continued advances are, in part, hampered by technology limitations associated with requirements for physical tethers that connect external equipment to rigid probes inserted into delicate regions of the brain. The results can lead to tissue damage and alterations in behavioral tasks and natural movements, with additional difficulties in use for studies that involve social interactions and/or motions in complex 3-dimensional environments. These disadvantages are particularly pronounced in research that demands combined optogenetic and pharmacological functions in a single experiment. Here, we present a lightweight, wireless, battery-free injectable microsystem that combines soft microfluidic and microscale inorganic light-emitting diode probes for programmable pharmacology and optogenetics, designed to offer the features of drug refillability and adjustable flow rates, together with programmable control over the temporal profiles. The technology has potential for large-scale manufacturing and broad distribution to the neuroscience community, with capabilities in targeting specific neuronal populations in freely moving animals. In addition, the same platform can easily be adapted for a wide range of other types of passive or active electronic functions, including electrical stimulation.

neuroscience | pharmacology | optogenetics

Neurological diseases affect the quality of life of millions of people worldwide (1). Emerging tools for the manipulation of neural activity in the deep brain create important avenues for basic research into the operation of neural circuits and the development of associated insights for the underlying causes and treatments of neurological diseases (1, 2). Pharmacology and optogenetics represent two highly informative and widely used approaches in neuroscience research (3–7). While facets of each technique have improved (e.g., more-selective drugs, uncaged ligands, light-sensitive proteins with varied on/off kinetics), the chronic implant and its connection to a secondary tethered system for drug/light delivery have effectively remained unchanged (3). The hardware associated with these approaches can 1) in-

troduce damage to fragile tissues during implantation, 2) result in irritation at the device/tissue interface, 3) affect studies of natural behaviors of untethered, freely moving animals, 4) frustrate investigations of social interactions due to entanglements, and 5) prevent

Significance

Neuroscience studies using optogenetics have greatly improved our understanding of brain circuits. Advances in the combined use of optogenetics and pharmacology to further probe important neurochemical signals has lagged, however, in large part due to the inconvenience of conventional cannulated approaches, as well as the difficulty in controlling, powering, and manufacturing optofluidic devices that are reliable and scalable for distribution to the neuroscience community. Here, we present a battery-free, wireless, lightweight optofluidic device that allows adjustable infusion rates, hands-free operation, and unlimited power supply, and is compatible with existing near-field communication (NFC) technology. We show that this device not only reproduces optogenetic and pharmacological experiments in vivo but, additionally, allows far greater freedom of movement in small animal models compared to existing, comparable platforms.

movements in complex 3-dimensional environments (8–12). These drawbacks, coupled with recent advances in flexible electronics and microfluidics (13–15), provide strong motivation for the development of innovative engineering platforms to improve experimental fidelity and expand the possibilities for advanced brain research studies in awake, behaving animals.

In addition to improving the technology for optogenetic and pharmacological studies, there is a growing interest in combining different or multiple methodologies for neuronal circuit manipulation. For example, optogenetics and fiber photometry or miniaturized microscopy combine light and genetics to both control and monitor neurons in vivo (16). Studies using such techniques indicate that different optogenetic stimulation parameters engage different neurotransmitter systems (17), and modulate different neuronal ensembles during discrete behavioral epochs (18). Although sophisticated and powerful in dissecting circuit activity, these combined platforms are constrained by the inability to cohesively incorporate pharmacology, thereby leaving many of the neurochemical mechanisms driving changes in behavior or neural activity unresolved (16). This limitation can be overcome by using systems that combine independently controlled pharmacological and optogenetic functions within a single platform. Ideally, such devices would be wirelessly controlled, programmable, soft, and lightweight to adapt to any experimental design while also avoiding damage to brain tissue or disruption of behaviors of freely moving animals.

In 2015, we introduced a wirelessly controlled optofluidic device for delivery of both fluidic compounds and optogenetic stimulation (19). Although an important advance, the device retained several nonideal features, including a battery-powered, thermal–mechanical micropump, nonnegligible heat generation (~87 °C) during the operation, limited lifetimes, inability to reuse the device, complexity in system design, and absence of accessibility beyond specially trained laboratories. Recent advances offer options in wireless drug delivery, with or without optogenetic functionality, that bypass certain drawbacks associated with the traditional cannula approach, but most are still constrained by requirements for 1) rigid stainless steel channels and large feature sizes (weight > 6.6 g; dimension > 14.4 mm × 15 mm × 24.8 mm) and 2) wireless operation in radio frequency (RF) bands that are sensitive to signal reflection, interference, and absorption by biological tissue, metallic objects, water features, and other obstructions (6, 20).
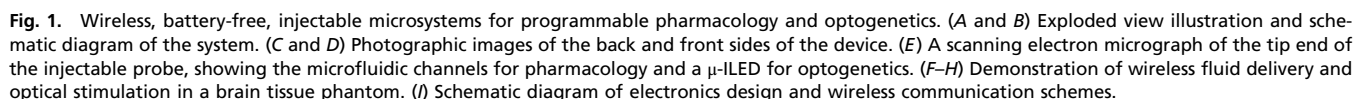
Recently, we introduced a soft, fully implantable optofluidic cuff system designed to deploy on peripheral nerves, with ultralow power requirements by use of miniaturized electrochemical micropumps for drug delivery (21). Here, we improve upon and adapt those ideas to establish a functional device that is able to interface with the brain. The resulting system maintains the same ultralow power operation and wireless, battery-free functionality, but also includes additional capabilities in drug refillability and programmable control over flow rate. Lastly, the design of the device is compatible with existing large-scale manufacturing practice, further underscoring its potential for widespread use across the neuroscience community. The system is 1) refillable and reusable; 2) capable of independent, multimodal operation through the infusion of multiple types of drugs and/or the delivery of optical stimulation; 3) lightweight (0.29 g) and compact in its construction; and 4) entirely wireless, with battery-free operation, thereby bypassing the physical burden normally imposed by larger implantable devices. The results described in the following demonstrate multiple ways in which this easy-to-use device and control platform can be broadly applied to behavioral conditions used in modern neuroscience research. Collectively, this device represents an important advance in wireless optofluidic technology for neuroscience in a format that is accessible and practical.

Results

Device Design and Operational Features. The microsystem detailed here includes a wireless, battery-free electronics module, 4 miniaturized electrochemical micropumps and reservoirs, a thin (~100 μm), soft (modulus ~3 MPa) microfluidic probe for fluid delivery, and a microscale inorganic light-emitting diode (referred to here as μ-ILED, 270 μm × 220 μm × 50 μm) light source for optogenetics (Fig. 1). A refilling port (diameter ~350 μm) on the sidewall of each reservoir allows for multiple fluidic infusions with the same device. Fig. 1 *A* and *B* presents schematic diagrams of a complete system that integrates each of these components together with a magnetic loop antenna for wireless power harvesting via magnetic resonant coupling protocols. The design is fully compatible with our recent wireless electronic platform and control software for the optogenetics (22). Fig. 1 *C* and *D* shows optical images of front side and backside views. Fig. 1*E* presents a scanning electron microscope (SEM) image of the injectable tip end of a probe that includes one μ-ILED for optical stimulation/inhibition and 4 microchannels for the programmable delivery of up to 4 drugs. Demonstration experiments using colored dyes and phantom brain tissues (0.6% agarose gel) illustrate the operation. Following a wirelessly triggered event, the microcontroller (μC) in the electronics module activates a selected electrochemical micropump to initiate fluidic delivery or the μ-ILED for optogenetic stimulation/inhibition, or both simultaneously (Fig. 1 *F–H*). A red indicator LED provides a convenient indication for the operation of device. The miniaturized dimensions (radius 0.5 cm; thickness ~0.4 cm), the lightweight construction (~0.29 g; *SI Appendix*, Fig. S1 *A* and *B*), wireless, programmable operation, and the mechanical compliance of the probes represent key characteristics, as detailed below.

Magnetic resonant coupling at 13.56 MHz transfers power wirelessly to the device from a primary antenna that encircles the area of interest (Fig. 1*I*), thereby eliminating the need for a battery and its associated bulk and weight. These magnetically coupled antennas operate in the high-frequency (HF, 3 MHz to 30 MHz) band to enable full wireless coverage across many cage types and environments, with little sensitivity to the presence of objects or physical obstructions, including those environments that involve metal plates, cages, or meshes or those with water pools, baths, or mazes (22). This same wireless link supports a programmable control strategy through a graphical user interface on a computer. Wireless control relies on a custom protocol based on on–off keying, as schematically outlined in Fig. 1*I*, with a predetermined parameter set, as described in detail in ref. 23. This scheme enables digital control over optogenetic stimulation frequency, duty cycle, and pumping parameters. *SI Appendix*, Fig. S1 *C* and *D* shows the complete system, which includes a computer with customized control software, a multicomponent power distribution control box, an antenna tuner, and a customizable transmission antenna.

Electrical, Fluidic, and Optical Characterizations. A thin, flexible printed circuit board (PCB) supports the electronic components for this system, including a μC, capacitors, rectifiers, and an RF antenna (Fig. 1 *B* and *C* and *SI Appendix*, Fig. S2 and Table S1). Here, a capacitor of 75 pF tunes the secondary antenna to 13.56 MHz (*SI Appendix*, Fig. S3A). *SI Appendix*, Fig. S3B shows the rectification behavior with decreasing ohmic loads. Peak power of over 18 mW is achieved at a voltage of 11 V and a load of 6.8 kohm at the center of a home cage with 6W input power. Harvested power changes with relative angle to the primary coil, shown by the unrectified power decreasing with increasing angle in *SI Appendix*, Fig. S3C. Fig. 2*A* shows the power distribution as a function of position in a 25 × 25 cm conditional place preference (CPP) cage powered at 6 W at physiologically relevant heights of 3 and 6 cm. Power distribution for a home cage powered at 6 W is

Zhang et al.

Fig. 1. Wireless, battery-free, injectable microsystems for programmable pharmacology and optogenetics. (*A* and *B*) Exploded view illustration and schematic diagram of the system. (*C* and *D*) Photographic images of the back and front sides of the device. (*E*) A scanning electron micrograph of the tip end of the injectable probe, showing the microfluidic channels for pharmacology and a μ-ILED for optogenetics. (*F–H*) Demonstration of wireless fluid delivery and optical stimulation in a brain tissue phantom. (*I*) Schematic diagram of electronics design and wireless communication schemes.

also in Fig. 2*B*. Minimum power outputs of 11 and 18 mW occur at the center of the CPP cage and home cage, respectively. The power distributions for lower RF powers are shown in *SI Appendix*, Fig. S3 *D* and *E*. Fig. 2*C* summarizes a characterization study

of the power consumption of the device. Here power consumption varies with time and is modulated by duty cycle and modality. Fig. 2*C* shows data for 3 states: low power mode of the μC (0.04 mW and peak power of 0.40 mW), μ-ILED active (0.38 mW and
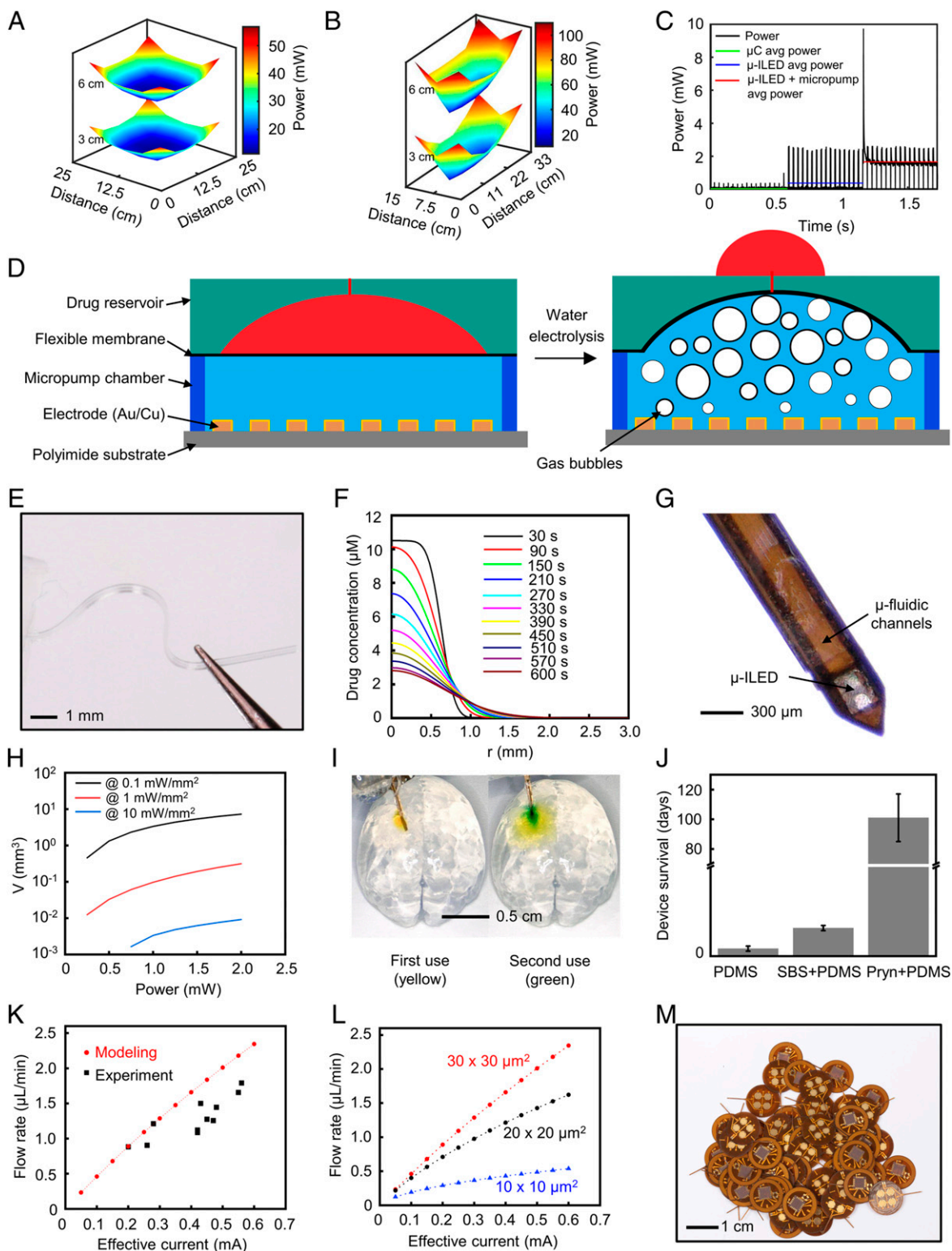
Fig. 2. Electrical, optical and fluidic characterization results. (*A*) Rectified power at the implant measured in a 25 cm × 25 cm behavioral chamber with 6W input power at implant heights of 3 and 6 cm with respect to cage floor. (*B*) Rectified power at the implant measured in a 15 cm × 33 cm home cage with 6W input power at implant heights of 3 and 6 cm with respect to cage floor. (*C*) Power consumption of implant with input voltage of 3.3 V for multiple states including a low-power μC idle state, μ-ILED with 10 mW/mm² irradiance output at 30 Hz, and simultaneous μ-ILED and drug micropump activation. (*D*) Schematic diagram of the electrochemical micropump based on water electrolysis. (*E*) Picture that illustrates the soft, compliant mechanics of the microfluidic probe. (*F*) Distribution of drug concentration along radial direction for *t* = 30, 90, 150, 210, 270, 330, 390, 450, 510, 570, and 600 s. (*G*) Optical micrograph of an integrated optofluidic probe. (*H*) Effective illumination volume at 3 different irradiance thresholds and input optical powers from 0.25 mW to 2 mW. (*I*) First and second use of a device, demonstrating the ability to refill and reuse the microfluidic system. (*J*) Device survival lifetime in 1× PBS at 37 °C when encapsulated with a monolayer of PDMS alone, a bilayer of SBS and PDMS, or a bilayer of Pryn and PDMS. (*K*) Maximum flow rate in a microfluidic channel (cross-sectional area of microchannel ~30 × 30 μm²) as a function of effective current. (*L*) Geometry-dependent maximum flow rate in microfluidic channels as a function of effective current. (*M*) Picture of devices manufactured using flexible PCB technology.

peak power of 2.5 mW with a duty cycle of 13.5%, and stimulation frequency 30 Hz), and micropump in conjunction with the μ-ILED (1.66 mW and peak power of 2.5 mW, μ-ILED duty cycle 13.5%, micropump duty cycle 86.5%, and stimulation frequency 30 Hz). The initial power consumption peak when activating the micropump can be attributed to the initiation of the electrochemical process and the capacitive nature of the interdigitated electrode structure. The average power consumption is well below harvesting capabilities for both the 25 × 25 cm CPP cage and the home cage, resulting in a tolerance to conditions such as rearing, which results in an increased implant angle with respect to the primary antenna. For experiments where small variations in output power and system voltage are not tolerable, an actively regulated system can be achieved via the integration of a low dropout voltage linear regulator (23). An example is shown in *SI Appendix*, Fig. S3F, where the output voltage with a load that represents the device under simultaneous electrochemical pumping and μ-ILED stimulation.

The miniaturized electrochemical micropump serves as an alternative to previously reported thermally activated versions (19, 21, 24–27). This approach allows for low power operation (<1 mW), negligible heat generation (<0.2 °C), high delivery efficiency (~90%) of the fluid housed in the reservoirs, simple construction, and large driving force (21). Each reservoir has an associated pumping chamber (cylinder shape; height 1 mm; diameter 2.45 mm, *SI Appendix*, Fig. S4), a set of interdigitated electrodes (Au/Cu, thickness 200 nm/18 μm, ~50 μm width, ~50 μm space), and a flexible separating membrane of polystyrene-block-polybutadiene-block-polystyrene (SBS) (Fig. 2D). At room temperature, pressure from the water hydrolysis reaction deforms a flexible membrane, thereby driving the flow of pharmacological agents out of the reservoir to the targeted area of the brain through corresponding microfluidic channels (Fig. 2D). The micropump chamber and reservoir are both milled from a block of cyclic olefin copolymer (thickness: 1 mm), selected for its efficiency as a moisture barrier (water vapor permeability ~0.045 g·mm/m²·d at 23 °C and 85% relative humidity) and resistance to hydrolysis, acids, alkalis, and polar solvents such as methanol, ethanol, acetone, and isopropanol (28), thereby allowing use of drugs that are soluble in water, dimethyl sulfoxide, ethanol or sodium hydroxide (50%). A bilayer of Ti/SiO$_2$ (5 nm/20 nm) deposited by sputtering (AJA International) renders the surface of the SBS film hydrophilic. The positively charged drug molecules may attach on the surface of the drug reservoir because of electrostatic interactions. This issue can be solved by functionalizing with a positive amine group.

Here, the flexible membrane of SBS offers a combination of soft mechanical characteristics (modulus ~13 MPa) and effective barrier properties (water permeability 8.52×10^{-8} g·m/m²·h·Pa; oxygen permeability 11.88 barrier; hydrogen permeability 21.66 barrier) (21). Each microchannel lies along the length of a thin (~100 μm), mechanically soft, and flexible (modulus ~3 MPa) probe (4 channels, each with 10×10 μm² cross-sectional areas) for minimally invasive, targeted fluid delivery into targeted regions of the deep brain (Fig. 2E and *SI Appendix*, Fig. S5 A and B). Previous studies quantified the "functional" spread of a drug by measuring changes in Fos activity (29–32). *SI Appendix*, Table S2 shows a few examples of this analysis for injection volumes sized similarly to our device. Overall, the functional diffusion volume is in the range between 0.05 and 3.92 mm³. An analytical model of drug diffusion into the brain tissue following wireless infusion captures the physics. The injected drug is modeled to have initial uniform distribution with concentration C_0 in a sphere of radius r_0 in the brain tissue. With an extracellular space fraction of the brain of $\alpha = 0.21$ (33), and injected volume of 0.25 μL at 50 μM concentration of drug in a typical pharmacology study, $C_0 = 10.5$ μM and $r_0 = 0.66$ mm. With a given diffusion coefficient, the model provides a quantitative prediction

of the distribution of drug concentration after wireless microfluidic delivery. For diffusion of small molecules, Fig. 2F shows the drug concentration distributed along the radial direction at $t = 30$, 90, 150, 210, 270, 330, 390, 450, 510, 570, and 600 s for D-2-amino-5-phosphonovalerate acid (D-APV), a widely used competitive N-methyl-D-aspartate (NMDA) antagonist, with apparent diffusion coefficient $D = 2.8 \times 10^{-6}$ cm²·s⁻¹ (34), and the contours of concentration are shown in *SI Appendix*, Fig. S5C. For diffusion of macromolecules into brain, *SI Appendix*, Fig. S5 D and E show the diffusion of NGF, a 26.5-kDa nerve growth factor protein, with apparent diffusion coefficient $D = 2.95 \times 10^{-7}$ cm²·s⁻¹ (35). Integration of the probe into these calculations will yield different distributions of drug concentration, as the substrate of the probe prevents the diffusion to its backside (Fig. 2G).

The soft microfluidic probe has a width of ~350 μm (cross-sectional area: 0.035 mm²). These dimensions are much smaller than those of conventional 26-gauge metal cannulas, where the diameters are 460 μm (cross-sectional area: 0.166 mm²). The probe also integrates an μ-ILED system with similar overall geometry to provide functionality relevant for optogenetics (22), in vivo optopharmacology, or other applications that require light sources (36, 37) (Figs. 1E and 2G). RF coupling of the primary antenna to the secondary antenna on the injectable microsystem results in harvested electrical powers ranging from 11 mW to 115 mW (Fig. 2 A and B). The harvested power operates the μC and μ-ILED, which typically requires an average electrical power of 0.38 mW (Fig. 2C). Electrical power to the μ-ILED is regulated through a current limiting resistor, resulting in a controlled conversion to optical stimulation output (23). In this configuration, optical powers of 0.25 mW to 2 mW can be realized, with corresponding irradiances ranging from 4.21 mW/mm² to 33.67 mW/mm², at the μ-ILED's surface, and produce illumination volumes from 0.012 mm³ to 0.315 mm³, respectively, at 1 mW/mm² illumination threshold (Fig. 2H and *SI Appendix*, Fig. S6 and Table S3 provide μ-ILED illumination volume of brain tissue predicted by Monte Carlo simulations). Irradiance output is well within typical optogenetic parameters of 1 mW/mm² to 10 mW/mm².

Drug Refillability. Fig. 2I highlights the ability to refill and reuse the reservoir. The electrochemical pumping mechanism and refilling ports on the sides of the reservoirs allow multiple cycles of use, thereby enabling studies over long periods of time with multiple drug delivery events. Here, a Hamilton syringe or 30G needle attached to a 1-mL syringe allows loading of electrolyte (50 mM potassium hydroxide, KOH, or 50 mM sodium hydroxide, NaOH) and drug into the micropump chamber and reservoir, respectively, through the refilling ports (*SI Appendix*, Fig. S7). Sealing the ports with a removable layer of silicone elastomer (Kwik-Sil; World Precision Instruments) or paraffin wax prevents leakage or evaporation. The power consumption–voltage characteristics and the maximum displacement of the flexible membrane serve as additional means to quantify the performance after refilling and resealing. The results, shown in *SI Appendix*, Figs. S8 and S9, indicate negligible difference (<10%) for the first, second, and third uses. The flow rate depends on the power applied to the electrochemical micropumps (power consumption–voltage characteristics), the deformation of flexible membrane, and the sizes of microfluidic channels. Since the refilling does not change the geometry of the microfluidic channels, these measurements suggest a stable flow rate of devices for reuse.

Device Encapsulation. A bilayer coating of Parylene C and polydimethylsiloxane (PDMS) encapsulates the associated wireless electronics and μ-ILED probe. Fig. 2J shows the survival lifetime of injectable part of the μ-ILED probe (6 mm long, adjustable to match the targeted brain region) in 1× phosphate-buffered saline (PBS) at 37 °C when encapsulated with a single layer of PDMS

(dip-coating, mixed at 10:1 ratio, ~20 μm thick), a bilayer of SBS (4 g/40 ml in toluene, dip-coating, ~20 μm thick) and PDMS (dip-coating, mixed at 10:1 ratio, ~20 μm thick), and a bilayer of Parylene C (Pryn, chemical vapor deposition, ~5 μm thick) and PDMS (dip-coating, mixed at 10:1 ratio, ~20 μm thick). Although ultrathin, transferred layers of thermally grown silicon dioxide can provide superior barrier characteristics under physiological conditions (38, 39), an encapsulation lifetime of about 100 d is sufficient for most optogenetic studies, considering the optimal period of testing for virally expressed opsins and age of the test animal.

Programmable Control over Flow Rate. Control of the rates of delivery can be important in many neuroscience studies. Excessively high rates may induce tissue damage, while insufficient rates may increase the potential for blockage at the exit ports of soft microfluidic channels. The rates of gas generation during electrochemical pumping determine the delivery rates. The pumping rate under constant current operation can be roughly written as (40)

$$Q = \frac{3}{4} \frac{i}{F} V_m,$$ [1]

where i is the current applied to the electrodes, F is Faraday's constant, and V_m is the molar gas volume at 25 °C and atmospheric pressure. This equation suggests that the rate can be controlled most easily through the time-averaged applied current (effective current), or, more specifically, in practice, the duty cycle of the pulse width modulation current. However, due to 1) the flow resistance in microfluidic channel, and 2) the resistance from the stiffness of the flexible membrane, the actual flow rate is typically lower than the value predicted by Eq. **1**, and a more accurate model must be used to predict the pumping rate. Fig. 2K shows the maximum flow rates of a device inserted into a brain phantom (0.6% agarose gel) and operated at 3 V as the wireless transmitted power serves as a constant voltage source, with pulses at 490 Hz and various time-averaged applied currents. In modeling, constant time-averaged applied current is assumed during the operation of the electrochemical pumping process, and the predicted flow rate matches well with experiments when small current is applied. However, the gas bubbles generated during the electrochemical pumping reduce the contact area between the electrolyte solution and the interdigitated electrodes, thereby causing a decrease in applied current and, therefore, a mismatch between experiment and modeling at higher applied currents (Fig. 2K and *SI Appendix*, Table S4). *SI Appendix*, Table S5 shows the relationship between applied current and time required to reach maximum flow rate or total time to deliver >80% of fluid housed in the reservoir, which could be important for time-sensitive experiments. Importantly, the maximum infusion rates also depend on channel size, which can be customized (Fig. 2L). We note that microfluidic channel sizes of 30 × 30 μm² (cross-sectional areas) minimize the potential for blockage in in vivo studies.

Compatibility with Large-Scale Manufacturing Practice. The components and systems described previously form the foundations for a manufacturable, low-cost device for wireless programmable pharmacology and optogenetics that can be used by neuroscientists with little or no background in RF electronics. The designs align with standard manufacturing practice in electronics, fluidics, and microsystems technologies. Specifically, the fabrication exploits scalable techniques such as laser structuring and microfabrication, using equipment readily available in academic laboratories. Manufacturing of each subsystem can occur in an automated process using flexible PCB technology and microfluidics. Results of an exploratory manufacturing procedure for the wireless power

supply, control electronics, and electrodes for the electrochemical micropumps appear in Fig. 2M and *SI Appendix*, Fig. S10.

Implanting Devices in the Brain. The process for surgical insertion of the device is similar to that of a conventional guide cannula or optic fiber. *SI Appendix*, Fig. S11 illustrates the steps for implanting the needle portion of the device into the brain and fixing the body of the device to the top of the skull. Briefly, an incision is made on top of the skull, and a small craniotomy is performed to allow probe insertion. The top of the device is mounted to a stereotaxic arm with a flat surface, and gently lowered into the brain. A small amount of medical device adhesive (Prism Medical Device Adhesive, 4541; Loctite) is applied near the point of insertion, bonding the needle to the skull. When the adhesive is fully hardened, the stereotaxic arm is raised while the secured device remains attached to the skull. *SI Appendix*, Fig. S11 G and H shows that the mice are in good health and that the devices cause no obvious adverse effects at 3 d and 30 d after surgery, respectively. Implantation does not disrupt normal locomotion, even as soon as 3 d after surgery. The high degree of mechanical compliance and the minimal tissue displacement associated with the probes are highlighted via some reduced lesioning and immunoreactive glial responses compared to those associated with conventional metal cannulas (Fig. 3). These findings are consistent with those of other thin, flexible deep brain implants (7, 19).

Wireless Pharmacology. This system operates with a remotely controlled interface to independently infuse multiple fluids in various environments, such as home cages or behavioral testing chambers. To test the operability of these devices in the deep brain across multiple test sessions, we targeted the brainstem ventral tegmental area (VTA) of wild-type (C57BL/6J) mice (Fig. 4A). Previous studies show that unilateral opioid stimulation in the VTA causes a stereotypical increase in locomotion and/or turning behavior in which the animals spin 360° in the contralateral direction relative to the hemisphere of injection (Fig. 4B) (19). We recapitulated these studies by wirelessly triggering the delivery of artificial cerebrospinal fluid (ACSF) as a vehicle control or the mu opioid receptor agonist [D-Ala²,N-Me-Phe⁴,Gly-ol⁵]-enkephalin (DAMGO) into mice 7 d following surgical implantation. Drug conditions were counterbalanced across mice, and infused via the same drug reservoir. While the device has the capability to infuse up to 4 drugs through its 4 separate reservoirs, we chose to demonstrate the reusability and refillability of the reservoirs by using the same reservoir for both test days. Specifically, mice were gently placed into a home cage−sized chamber and immediately received a wireless infusion of the ACSF or DAMGO. Mice were allowed to freely move in the chamber for the duration of the infusion (~2 min). After 4 min in the chamber (to allow full diffusion of the drug), mice were moved directly into an open field chamber (50 cm × 50 cm) where they were allowed to freely explore for 1 h (Fig. 4C). At the end of the hour session, mice were removed from the open field and placed back into their home cage. To record locomotor and rotation behaviors, a camera was mounted to the ceiling, and total distance traveled was recorded. Total number of contralateral turns was scored offline by an observer blind to the test condition. There was no obvious change in the overall locomotor behavior after vehicle or DAMGO infusions (Fig. 4D). As predicted, however, DAMGO stimulation led to a doubling of the number of stereotypical rotations compared to the ACSF test day (Fig. 4E) (Wilcoxon, $P = 0.031$, Cohen's $d = -0.64$). While previous demonstrations of this experiment have shown both locomotor and rotation effects of DAMGO (19), the differences here could be related to the lightweight nature of this device (0.29 g vs. 1.855 g). Previous reports using a battery-operated optofluidic device showed substantially lower baseline locomotion compared

Fig. 3. Device implantation impact on the brain. (*A*) Schematic and mouse brain library atlas. Red spot indicates approximate implantation site. (*B*) Mean ± SEM cross-sectional area of lesions from cannulas and optofluidic probes (Student's *t* test, ****$P < 0.0001$, *n* = 3/group). (*C*) Representative linescan of fluorescence intensity from cannula (black) and optofluidic probe (red) lesions. (*D–K*) Representative confocal fluorescence images of horizontal striatal slices show immunohistochemical staining for DAPI (blue), astrocytes (GFAP, red), and activated microglia (Iba1, green) and overall lesion from a cannula and an optofluidic device. All histological and confocal settings were kept consistent across groups. Lesioned tissue from either cannula (*Top*) or device (*Bottom*) implantation is outlined in white dashed lines. (Scale bars, 100 μm.)

to this device (19), and even the DAMGO stimulated locomotion often only reached the baseline locomotor activity observed in mice implanted with this device. These differences highlight how the weight of a head-mounted device can dramatically affect normal behavior.

Wireless Optogenetics. To evaluate whether the optogenetic capabilities of the device would also work in deep tissue, we stimulated local GABAergic neurons in VTA expressing channelrhodopsin (ChR2) in a real-time place test (RTPT) (Fig. 4 *F* and *G*) (41). Previous reports have shown that GABA neuron stimulation is aversive, reduces responding for rewards, and is actively avoided (41, 42). First, vGAT-cre mice received an injection of AAV5-EF1a-DIO-hCHR2-(H134R)-eYFP into the VTA. Two weeks later, mice were implanted with the device, then allowed to recover for 1 week before behavioral testing. Mice were tested in a 20-min RTPT, in which they were able to freely roam between 2 indistinguishable chambers (Fig. 4*H*). Each mouse was tested twice. On one test day, they never received stimulation. On the other test day, they received stimulation in one chamber, but not the other. Time spent in each chamber was calculated to determine an overall preference score for each day. As expected, mice

showed a robust avoidance of the stimulation-paired chamber, spending ~15% less time in the stimulation side compared to the nonstimulated test day (Wilcoxon test, $P = 0.031$, Cohen's $d = 2.05$) (Fig. 4 *I* and *J*). This aversion did not appear to be due to changes in locomotor activity between the stimulated and nonstimulated test days (total distance, $P = 0.103$; velocity, $P = 0.103$) (Fig. 4*K*). Like the DAMGO-stimulated rotations experiment, these mice showed demonstrably higher general locomotion compared to previous wireless optofluidic models, and results are comparable to traditional tethered optogenetic studies (19, 41). These results demonstrate that the wireless optofluidic devices can activate neurons in vivo while mice perform a frequently used behavioral assay.

Combining Wireless Pharmacology and Optogenetics in Vivo. One of the most compelling uses for this optofluidic device is to combine pharmacology and optogenetics. Here, we sought to determine whether this device was capable of effectively integrating these two approaches. We first injected a panneuronal channelrhodopsin expressing virus into dorsal hippocampus (DH) (Fig. 5 *A* and *B*). Three weeks later, we implanted the device into the same site. After 3 d of recovery from surgical implantation, animals
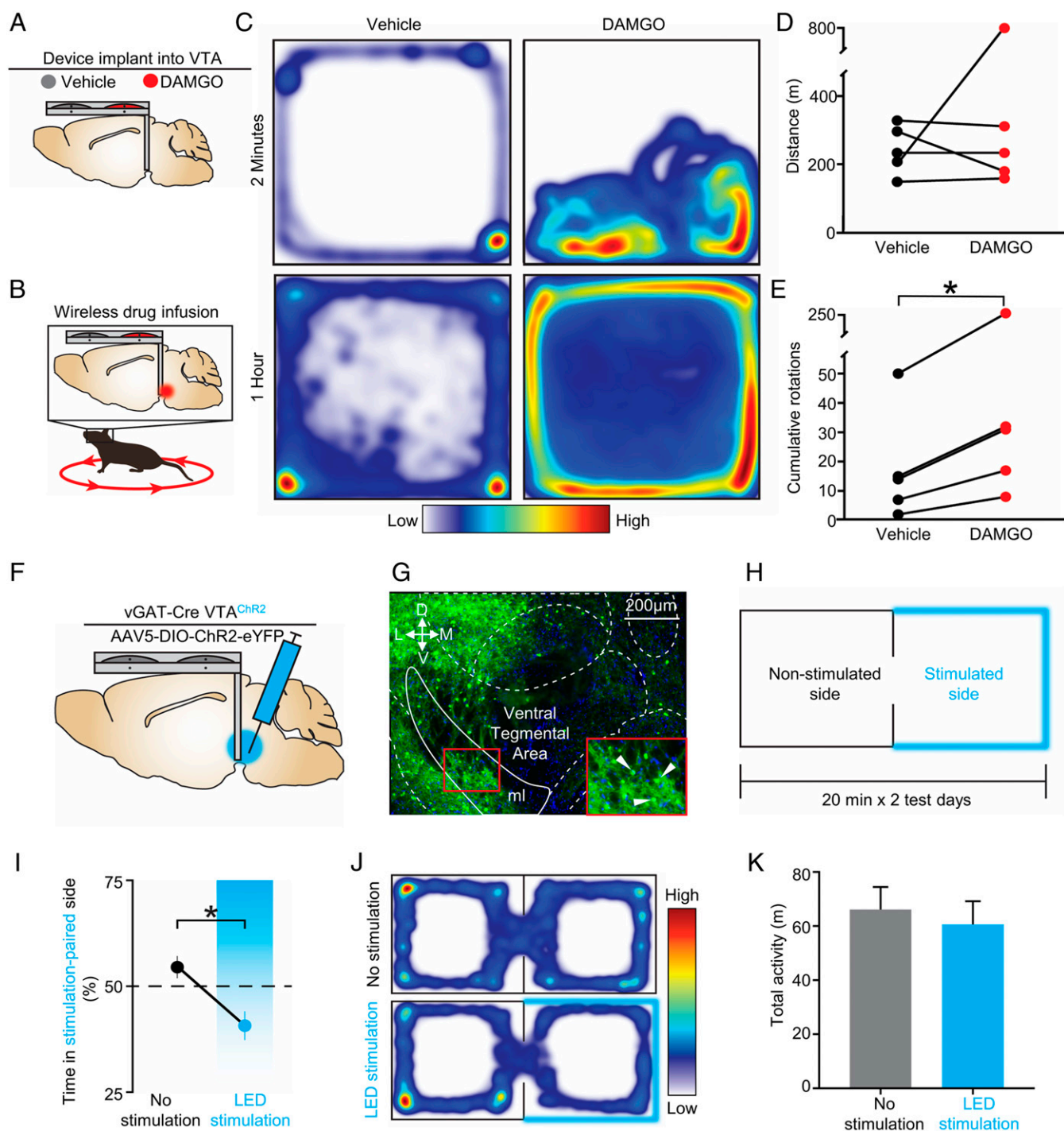
Fig. 4. Deep tissue demonstrations of in vivo wireless delivery of fluidic compounds and optogenetic stimulation of neurons. (*A* and *B*) Schematic of the fluid delivery and subsequent contraversive rotations. (*C*) Representative traces of movement from the same animal over the course of 2 min and 1 h after either vehicle or DAMGO infusions. (*D*) Overall locomotor behavior after vehicle or DAMGO infusions. (*E*) Cumulative contraversive rotations after vehicle or DAMGO infusions (*$P < 0.05$ Wilcoxon test). (*F*) Schematic of viral injection of channelrhodopsin into vGAT-cre mice. (*G*) Representative image showing robust viral infection in VTA. White arrows indicate individual infected neurons. (*H*) Schematic of Real-Time Place Test. (*I*) Optogenetic stimulation of VTA GABA neurons causes a place avoidance (*$P < 0.05$ Wilcoxon test). (*J*) Representative trace of cumulative time spent in each zone on test day with no stimulation (*Top*) versus stimulation (*Bottom*). (*K*) Optogenetic simulation did not disrupt overall locomotor activity.

were habituated in a chamber similar in size to their home cage, in which they were able to freely explore for 2 min (day 1). On day 2, the animals were again placed in the chamber and allowed to explore for 2 min. At the onset of the second minute, mice received optical stimulation for 1 min, and locomotor activity was recorded

(Fig. 5*C*). Here we show that 4-Hz stimulation of DH results in a significant increase in locomotion (*t* test, $P = 0.023$) (Fig. 5 *D* and *E*). In a subsequent, counterbalanced experiment, wireless pharmacological delivery of an NMDA receptor antagonist (APV) was given prior to the photostimulation. We found that pretreatment with
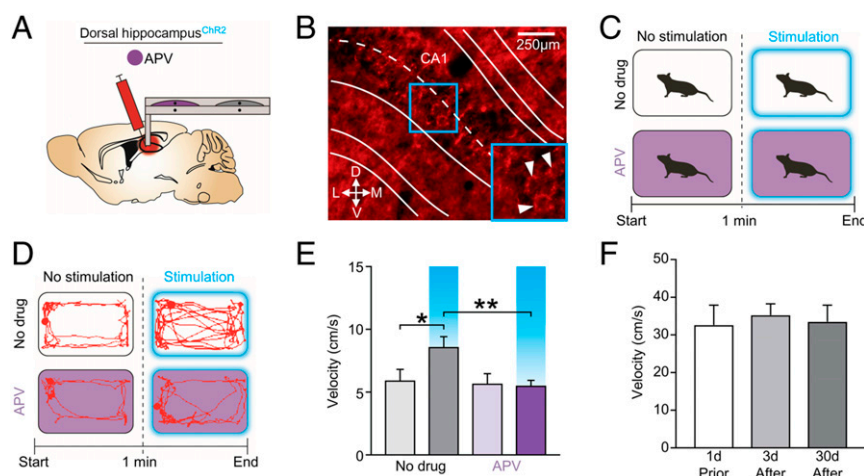
Fig. 5. Optogenetic stimulation of hippocampal neurons increases locomotion, and is blocked by the wireless infusion of the NMDA receptor antagonist APV. (*A*) Schematics of viral injection and the implantation of optofluidic device. (*B*) Fluorescent image showing expression of pAAV.CAG.hChR2(H134R)-mCherry.WPRE.SV40 in DH. Solid lines depict outline of hippocampal tissue, and dashed line indicates subdivisions within CA1. (*Inset*) Blue box in center of image is enlarged in right corner, with white arrows pointing to individual infected neurons. (*C*) Schematic of locomotor test, with and without optical stimulation or APV infusion (*D*) Representative traces of mice across experimental conditions. (*E*) The 4-Hz optical stimulation of DH increases locomotion (*$P < 0.05$, t test), and is blocked by the wireless infusion of APV (**$P < 0.01$, t test), $n = 7$ to 8. (*F*) Baseline locomotor activity prior to and after device implantation. Implantation does not disrupt normal locomotion, even as soon as 3 d after surgery ($n = 4$).

APV (wirelessly infused via the device) completely blocked optical stimulation-induced increases in locomotor activity (paired t test, $P = 0.0071$) (Fig. 5 *D* and *E*). These results are consistent with previous reports that photostimulation of neurons in DH causes a glutamate-dependent increase in locomotion (43–45), demonstrating that this device can effectively replicate a well-known optogenetic and pharmacological phenomenon. Notably, baseline locomotor activity was not affected by implantation of the device, even as soon as 3 d after surgery, nor were there any discernable deficits observed when behavior was recorded 30 d later (Fig. 5*F*). These results indicate that the optogenetically induced locomotion and the subsequent APV blockade function as expected, with no unusual or disruptive features preventing mice from behaving similarly to fiber or cannula implanted mice.

Discussion

The wireless, battery-free, injectable microsystem presented here represents a versatile technology for manipulation of deep brain tissue in freely moving animals. The platform offers multifunctional capabilities in a single, soft implant with options for in vivo wireless pharmacology and optogenetics, many of which would be impossible to reproduce with conventional metal cannulas and/or optical fibers (37). There are several benefits of this platform compared to existing technologies (*SI Appendix*, Table S6). First, fully wireless and battery-free operation eliminates the need for external or bulky connections to provide power for fluid or light delivery. The device is powered, controlled, and operated within the industrial, scientific, and medical radio band, and is highly compatible with widely available 13.56-MHz technology, thereby facilitating worldwide dissemination. The HF (3 MHz to 30 MHz) band antenna designs can be easily operated inside almost any environmental arena by novice operators, and are largely unaffected by the presence of objects or physical obstructions (e.g., walls, novel objects, bedding). In effect, this type of technology allows the device to be as functional as any currently available optical stimulation system (22, 42, 46–48), with the additional option of complementary pharmacology. Finally, since this device is directly and continuously powered through near-field communication (NFC) technology, there is no limit on power lifetime, thereby eliminating concerns about battery life/charging status during behavioral test sessions. This feature is especially

useful for studies that have extended time courses, such as overnight sleep studies or long-access (~6 h) self-administration sessions. Similarly, this device can be turned on and off at will or through transistor–transistor logic for more longitudinal studies without the need to interact with the animal at any time point during each test session.

Second, the lightweight construction (0.29 g, including reservoirs and micropumps, soft microfluidics, µ-ILED, and electronics for wireless power supply and control) bypasses physical constraints that can limit the natural movements of small animal models, allowing them to interact with the environment uninhibitedly. In fact, other drug delivery devices, with or without optogenetic functionality, are 6.4 to 22.8 times the weight of the device reported here (*SI Appendix*, Table S6), including the battery-operated device we have previously published (19). Such freedom is critical for many behavioral neuroscience studies (drug self-administration, social interactions) (49), where performance can be disrupted by stressful distractions or impediments (e.g., tethers, heavy weights). The battery-free operation allows the platform to operate with a much smaller feature size and weight than with battery power (the primary power source in other commercially available devices). The removal of an external battery and net reduction in device size (*SI Appendix*, Table S6) also allows our device to be implanted flush against the skull. This option enables unimpeded entry into nose ports and reward magazines in operant chambers, which can be difficult with some tethered protocols (extended tethers can prevent animals from triggering infrared beams or reaching rewards). These devices also lend themselves to locomotor tasks that can be difficult to test with tethered or bulky head mounts, such as wheel running, rotarod, or gait assays. Indeed, we observed a large difference in baseline locomotion between this device and other battery-powered iterations, indicating that weight alone is sufficient to greatly influence behavior. Using lighter, less obtrusive devices, like the one described here, will allow for greater versatility in behavior/optofluidic experiments.

Third, the device design uses a thin (~100 µm), soft (modulus ~3 MPa) microfluidic probe that avoids many of the issues in chronic inflammation and necrosis of neurons that are associated with traditional cannulas made of rigid materials like stainless steel (50). The thin geometry and soft mechanics adapt to brain

micromotions associated with physiological, behavioral, or mechanical sources (50). This behavior minimizes brain tissue damage during implantation and reduces the formation of glial scars for stable chronic operation (Fig. 3) (51). By our calculations, the area of lesioned tissue in a 26-gauge metal cannula that is 460 μm in diameter is ~0.184 mm^2, whereas the damage produced by our device is ~0.068 mm^2 (Fig. 3B). Perhaps even more striking, lesioned tissue from a thin optic fiber (~240 μm in dimeter) results in ~0.045 mm^2, indicating that our device produces comparable overall damage, but with double the functionality. Given that microglia can strongly impact neuronal activity (52, 53), features that minimize their recruitment, as found in our device, are critically important.

Fourth, multimodal operation permits independent infusions of multiple drugs or optical stimulation, for combined modes of use. The conventional approach in pharmacological and optogenetic experiments, such as optopharmacology, requires multiple tethers, tubing, and specialized commutators that can impede or make difficult otherwise straightforward experiments (37). With the system introduced here, separate tubing is no longer necessary, facilitating the execution and completion of behavioral studies. Eliminating tubes, injectors, commutators, and fiber optics reduces the number of steps, at which failure to perform can disrupt an experiment. Such a streamlined approach has gained traction in recent years, with several groups capitalizing on "single-step" optogenetics to minimize potential failures and maximize usability (54). Fittingly, our device is also capable of infusing viral vectors, allowing for more targeted optogenetic approaches. With the 4 available reservoirs, it would even be possible to infuse multiple viruses or tracers to further gain information on circuit dynamics or connectivity, in conjunction with causal optogenetic stimulations. The field of optopharmacology has made great strides in recent years, not only with the number of available compounds but also with the versatility of these compounds (37, 55). These advances are especially relevant for peptide neurotransmitter systems, which have historically been difficult to quantify in vivo. While some advances have been made in observing temporally distinctive peptide events (36), subminute time scales remain out of reach. Optopharmacology provides one means to tackle this issue by allowing investigators to infuse an inactive compound, then experimentally induce a peptide signal at a specific behaviorally relevant moment with optical stimulation. As newer compounds continue to be developed (e.g., bistable uncaging/recaging), the ability to simulate neurotransmitter signaling patterns in vivo will allow for exciting new ways to investigate neural systems. Therefore, having a device with both fluidic and optical capabilities will allow for the effective use of these compounds in vivo.

The system presented here is refillable and reusable. This design represents a major distinction compared to other available devices, and will encourage the adoption of combined optogenetic and pharmacology approaches into mainstream experimental designs. Traditionally, intracranial pharmacology is accomplished via the insertion of a microinjector through chronically implanted stainless steel cannulas. For experiments that require multiple injections, each insertion is accompanied by fresh injury to the brain, thereby limiting the total number of injections that can be performed. Our system is only implanted once, and the filling/refilling of the device is performed through the ports on the side wall of the reservoirs. In other words, this device bypasses the detrimental effects of multiple instances of acute tissue trauma while preserving the security of a chronically implanted fluid delivery system. An additional advantage is in the electrochemical pumping mechanism coupled with reaccessible drug reservoirs. Unlike other systems, in which experimenters are limited in the total number of infusions (e.g., traditional cannulations, optofluidic device published in 2015) (19), this device offers reusability beyond the 4 independent reservoirs already available, making it ideal for long-term experiments. For example,

it could be used for experiments that have multiple testable time points (e.g., fear extinction, drug sensitization, neurodegenerative diseases). Another potential use for the multiple reservoirs is the injection of multiple agents at the same time or at discrete time points during a test session (e.g., agonistic stimulation of a system followed by selective antagonism later in the same session). Regardless of the particular experiment, the adaptable user interface for controlling drug and/or light delivery allows for tailored experimental designs without having to reprogram the device. The freedom to program and initiate drug or light delivery, both of which our device accomplishes, is essential for an effective and widely usable device.

This platform also provides some potential as part of an integrated closed-loop system for in vivo recording and manipulation. For example, sensors might monitor neural activity or organ behaviors to guide control of a second system to enhance or disrupt those patterns (e.g., via optogenetic illumination) (56–59). Alternatively, the device and platform described here could be extended to include wireless photometric recordings of neural activity to guide localized pharmacological and/or optogenetic interventions (49). Similarly, genetically encoded receptor indicators could be combined with triggered drug release to quantify how the local neurochemical milieu affects receptor activity, with subsecond resolution (60). These and other possibilities provide multiple exciting avenues of study.

Overall, this lightweight optofluidic device with refillable/usable drug reservoirs, straightforward implantation procedures, an easy-to-use interface can accommodate wide-ranging experimental designs, and an essentially endless source of power via magnetic resonant coupling technology. The device is well suited for investigations of interactions between optogenetically activated circuits and subsequent neurochemical signaling, as well as for use with more advanced and cutting-edge technologies like optopharmacology. Because of its lightweight construction, it can be used in essentially any behavioral paradigm, as well as for either acute or long-term experiments. Its straightforward and streamlined manufacturing protocol also makes it readily accessible for nearly all engineering or neuroscience laboratories. Future iterations of the device could include multiple activatable LEDs, photometric sensing (49), or even more efficient NFC coupling to further boost its power output.

Materials and Methods

Details of fabrications and assembly of wireless optofluidic device, power characterization, theoretical modeling of drug diffusion, Monte Carlo simulations on brain tissue, and flow rate measurement and modeling appear in *SI Appendix*. Experimental animals, surgery, immunohistochemistry, immunoglial response in implanted tissues, and behavioral experiments are also in *SI Appendix*. All procedures were approved by the Animal Care and Use Committee of Washington University and Northwestern University and conformed to US National Institutes of Health guidelines.

Data and Materials Availability. All data needed to evaluate the conclusions in the paper are present in the paper and/or *SI Appendix* and Movie S1.

1. S. P. Lacour, G. Courtine, J. Guck, Materials and technologies for soft implantable neuroprostheses. *Nat. Rev. Mater.* **1**, 16063 (2016).
2. R. Chen, A. Canales, P. Anikeeva, Neural recording and modulation technologies. *Nat. Rev. Mater.* **2**, 16093 (2017).
3. K. Deisseroth, Optogenetics: 10 years of microbial opsins in neuroscience. *Nat. Neurosci.* **18**, 1213–1225 (2015).
4. K. Deisseroth, Optogenetics. *Nat. Methods* **8**, 26–29 (2011).
5. E. S. Boyden, F. Zhang, E. Bamberg, G. Nagel, K. Deisseroth, Millisecond-timescale, genetically targeted optical control of neural activity. *Nat. Neurosci.* **8**, 1263–1268 (2005).
6. C. Dagdeviren *et al.*, Miniaturized neural system for chronic, local intracerebral drug delivery. *Sci. Transl. Med.* **10**, eaan2742 (2018).
7. A. Canales *et al.*, Multifunctional fibers for simultaneous optical, electrical and chemical interrogation of neural circuits in vivo. *Nat. Biotechnol.* **33**, 277–284 (2015).
8. T. D. Y. Kozai *et al.*, Ultrasmall implantable composite microelectrodes with bioactive surfaces for chronic neural interfaces. *Nat. Mater.* **11**, 1065–1073 (2012).
9. I. R. Minev *et al.*, Biomaterials. Electronic dura mater for long-term multimodal neural interfaces. *Science* **347**, 159–163 (2015).
10. J. K. Nguyen *et al.*, Mechanically-compliant intracortical implants reduce the neuro-inflammatory response. *J. Neural Eng.* **11**, 056014 (2014).
11. S. I. Park *et al.*, Soft, stretchable, fully implantable miniaturized optoelectronic systems for wireless optogenetics. *Nat. Biotechnol.* **33**, 1280–1286 (2015).
12. T. I. Kim *et al.*, Injectable, cellular-scale optoelectronics with applications for wireless optogenetics. *Science* **340**, 211–216 (2013).
13. D. H. Kim *et al.*, Epidermal electronics. *Science* **333**, 838–843 (2011).
14. J. Heikenfeld *et al.*, Wearable sensors: Modalities, challenges, and prospects. *Lab Chip* **18**, 217–248 (2018).
15. A. Koh *et al.*, A soft, wearable microfluidic device for the capture, storage, and colorimetric sensing of sweat. *Sci. Transl. Med.* **8**, 366ra165 (2016).
16. L. A. Gunaydin *et al.*, Natural neural projection dynamics underlying social behavior. *Cell* **157**, 1535–1551 (2014).
17. E. Arrigoni, C. B. Saper, What optogenetic stimulation is telling us (and failing to tell us) about fast neurotransmitters and neuromodulators in brain circuits for wake-sleep regulation. *Curr. Opin. Neurobiol.* **29**, 165–171 (2014).
18. W. Xu, T. C. Südhof, A neural circuit for memory specificity and generalization. *Science* **339**, 1290–1295 (2013).
19. J. W. Jeong *et al.*, Wireless optofluidic systems for programmable in vivo pharmacology and optogenetics. *Cell* **162**, 662–674 (2015).
20. K. N. Noh *et al.*, Miniaturized, battery-free optofluidic systems with potential for wireless pharmacology and optogenetics. *Small* **14**, 1702479 (2018).
21. Y. Zhang *et al.*, Battery-free, fully implantable optofluidic cuff system for wireless optogenetic and pharmacological neuromodulation of peripheral nerves. *Sci. Adv.* **5**, eaaw5296 (2019).
22. G. Shin *et al.*, Flexible near-field wireless optoelectronics as subdermal implants for broad applications in optogenetics. *Neuron* **93**, 509–521.e3 (2017).
23. P. Gutruf *et al.*, Fully implantable optoelectronic systems for battery-free, multimodal operation in neuroscience research. *Nat. Electron* **1**, 652–660 (2018).
24. C. G. Cameron, M. S. Freund, Electrolytic actuators: Alternative, high-performance, material-based devices. *Proc. Natl. Acad. Sci. U.S.A.* **99**, 7827–7831 (2002).
25. A. Cobo, R. Sheybani, E. Meng, MEMS: Enabled drug delivery systems. *Adv. Healthc. Mater.* **4**, 969–982 (2015).
26. H. Gensler, R. Sheybani, P. Y. Li, R. L. Mann, E. Meng, An implantable MEMS micropump system for drug delivery in small animals. *Biomed. Microdevices* **14**, 483–496 (2012).
27. E. Meng, T. Hoang, MEMS-enabled implantable drug infusion pumps for laboratory animal research, preclinical, and clinical applications. *Adv. Drug Deliv. Rev.* **64**, 1628–1638 (2012).
28. T. Nielsen *et al.*, Nanoimprint lithography in the cyclic olefin copolymer, Topas, a highly ultraviolet-transparent and chemically resistant thermoplast. *J. Vac. Sci. Technol. B* **22**, 1770–1775 (2004).
29. A. Faure, S. M. Reynolds, J. M. Richard, K. C. Berridge, Mesolimbic dopamine in desire and dread: Enabling motivation to be generated by localized glutamate disruptions in nucleus accumbens. *J. Neurosci.* **28**, 7184–7192 (2008).
30. A. Faure, J. M. Richard, K. C. Berridge, Desire and dread from the nucleus accumbens: Cortical glutamate and subcortical GABA differentially generate motivation and hedonic impact in the rat. *PLoS One* **5**, e11223 (2010).
31. J. M. Richard, K. C. Berridge, Nucleus accumbens dopamine/glutamate interaction switches modes to generate desire versus dread: D(1) alone for appetitive eating but D(1) and D(2) together for fear. *J. Neurosci.* **31**, 12866–12879 (2011).
32. D. C. Castro, R. A. Terry, K. C. Berridge, Orexin in rostral hotspot of nucleus accumbens enhances sucrose 'liking' and intake but scopolamine in caudal shell shifts 'liking' toward 'disgust' and 'fear.' *Neuropsychopharmacology* **41**, 2101–2111 (2016).
33. C. Nicholson, Diffusion from an injected volume of a substance in brain tissue with arbitrary volume fraction and tortuosity. *Brain Res.* **333**, 325–329 (1985).
34. S. Bhattacharya *et al.*, NMDA receptor blockade ameliorates abnormalities of spike firing of subthalamic nucleus neurons in a parkinsonian nonhuman primate. *J. Neurosci. Res.* **96**, 1324–1335 (2018).
35. D. J. Wolak, R. G. Thorne, Diffusion of macromolecules in the brain: Implications for drug delivery. *Mol. Pharm.* **10**, 1492–1504 (2013).
36. R. Al-Hasani *et al.*, In vivo detection of optically-evoked opioid peptide release. *eLife* **7**, e36520 (2018).
37. S. Banala *et al.*, Photoactivatable drugs for nicotinic optopharmacology. *Nat. Methods* **15**, 347–350 (2018).
38. H. Fang *et al.*, Ultrathin, transferred layers of thermally grown silicon dioxide as biofluid barriers for biointegrated flexible electronic systems. *Proc. Natl. Acad. Sci. U.S.A.* **113**, 11682–11687 (2016).
39. H. Fang *et al.*, Capacitively coupled arrays of multiplexed flexible silicon transistors for long-term cardiac electrophysiology. *Nat. Biomed. Eng.* **1**, 0038 (2017).
40. R. Sheybani, E. Meng, "High efficiency wireless electrochemical actuators: Design, fabrication and characterization by electrochemical impedance spectroscopy" in *Micro Electro Mechanical Systems (MEMS), 2011 IEEE 24th International Conference*, (Institute of Electrical and Electronics Engineers, 2011), pp. 1233–1236.
41. K. R. Tan *et al.*, GABA neurons of the VTA drive conditioned place aversion. *Neuron* **73**, 1173–1183 (2012).
42. R. van Zessen, J. L. Phillips, E. A. Budygin, G. D. Stuber, Activation of VTA GABA neurons disrupts reward consumption. *Neuron* **73**, 1184–1194 (2012).
43. F. Fuhrmann *et al.*, Locomotion, theta oscillations, and the speed-correlated firing of hippocampal neurons are controlled by a medial septal glutamatergic circuit. *Neuron* **86**, 1253–1264 (2015).
44. A. Czurkó, H. Hirase, J. Csicsvari, G. Buzsáki, Sustained activation of hippocampal pyramidal cells by 'space clamping' in a running wheel. *Eur. J. Neurosci.* **11**, 344–352 (1999).
45. G. Buzsáki, Theta oscillations in the hippocampus. *Neuron* **33**, 325–340 (2002).
46. B. T. Saunders, J. M. Richard, E. B. Margolis, P. H. Janak, Dopamine neurons create Pavlovian conditioned stimuli with circuit-defined motivational properties. *Nat. Neurosci.* **21**, 1072–1083 (2018).
47. J. M. Otis *et al.*, Prefrontal cortex output circuits guide reward seeking through divergent cue encoding. *Nature* **543**, 103–107 (2017).
48. T. A. LeGates *et al.*, Reward behaviour is regulated by the strength of hippocampus-nucleus accumbens synapses. *Nature* **564**, 258–262 (2018).
49. L. Lu *et al.*, Wireless optoelectronic photometers for monitoring neuronal dynamics in the deep brain. *Proc. Natl. Acad. Sci. U.S.A.* **115**, E1374–E1383 (2018).
50. A. Gilletti, J. Muthuswamy, Brain micromotion around implants in the rodent somatosensory cortex. *J. Neural Eng.* **3**, 189–195 (2006).
51. H. Lee, R. V. Bellamkonda, W. Sun, M. E. Levenston, Biomechanical analysis of silicon microelectrode-induced strain in the brain. *J. Neural Eng.* **2**, 81–89 (2005).
52. G. M. Lewitus *et al.*, Microglial TNF-α suppresses cocaine-induced plasticity and behavioral sensitization. *Neuron* **90**, 483–491 (2016).
53. S. A. Liddelow *et al.*, Neurotoxic reactive astrocytes are induced by activated microglia. *Nature* **541**, 481–487 (2017).
54. S. Park *et al.*, One-step optogenetics with multifunctional flexible polymer fibers. *Nat. Neurosci.* **20**, 612–619 (2017).
55. M. R. Banghart, B. L. Sabatini, Photoactivatable neuropeptides for spatiotemporally precise delivery of opioids in neural tissue. *Neuron* **73**, 249–259 (2012).
56. A. D. Mickle *et al.*, A wireless closed-loop system for optogenetic peripheral neuromodulation. *Nature* **565**, 361–365 (2019).
57. A. Zhou *et al.*, A wireless and artefact-free 128-channel neuromodulation device for closed-loop stimulation and recording in non-human primates. *Nat. Biomed. Eng.* **3**, 15–26 (2019).
58. N. Wenger *et al.*, Closed-loop neuromodulation of spinal sensorimotor circuits controls refined locomotion after complete spinal cord injury. *Sci. Transl. Med.* **6**, 255ra133 (2014).
59. C. V. Latchoumane, H. V. V. Ngo, J. Born, H. S. Shin, Thalamic spindles promote memory formation during sleep through triple phase-locking of cortical, thalamic, and hippocampal rhythms. *Neuron* **95**, 424–435.e6 (2017).
60. T. Patriarchi *et al.*, Ultrafast neuronal imaging of dopamine dynamics with designed genetically encoded sensors. *Science* **360**, eaat4422 (2018).

ENGINEERING

NEUROSCIENCE

Supplementary Information for

Battery-free, lightweight, injectable microsystem for in vivo wireless pharmacology and optogenetics

Yi Zhang,[a,b,1] Daniel C. Castro,[c,1] Yuan Han,[d,e,f] Yixin Wu,[b] Hexia Guo,[b] Zhengyan Weng,[a] Yeguang Xue,[b,g,h] Jokubas Ausra,[i] Xueju Wang,[j] Rui Li,[k,l] Guangfu Wu,[a] Abraham Vázquez-Guardado,[m] Yiwen Xie[b], Zhaoqian Xie,[g,h,k] Diana Ostojich,[b] Dongsheng Peng,[n] Rujie Sun,[o] Binbin Wang,[p] Yongjoon Yu,[q] John P. Leshock,[b] Subing Qu,[r] Chun-Ju Su,[b] Wen Shen,[s] Tao Hang,[t] Anthony Banks,[b] Yonggang Huang,[b,g,h,m] Jelena Radulovic,[d] Philipp Gutruf,[i*] Michael R. Bruchas,[c,u,v*] John A. Rogers[b,m,w,x,y,z*]

[a]Department of Biomedical, Biological, and Chemical Engineering, University of Missouri, Columbia, MO 65211, USA.
[b]Department of Materials Science and Engineering, Northwestern University, Evanston, IL 60208, USA.
[c]Department of Anesthesiology and Pain Medicine, University of Washington, Seattle, Washington 98195, USA.
[d]Department of Psychiatry and Behavioral Sciences, Northwestern University, Chicago, IL 60611, USA.
[e]Department of Anesthesiology, Eye & ENT Hospital, Fudan University, 83 Fenyang Road, Shanghai 200031, China.
[f]Jiangsu Province Key Laboratory of Anesthesiology, Xuzhou Medical University, Xuzhou 221004, China.
[g]Department of Civil and Environmental Engineering, Northwestern University, Evanston, IL 60208, USA.
[h]Department of Mechanical Engineering, Northwestern University, Evanston, IL 60208, USA.
[i]Biomedical Engineering, College of Engineering, The University of Arizona, Bioscience Research Laboratories, 1230 N Cherry Ave., Tucson, Arizona 85721, USA.
[j]Department of Mechanical and Aerospace Engineering, University of Missouri, Columbia, MO 65211, USA.
[k]State Key Laboratory of Structural Analysis for Industrial Equipment, Department of Engineering Mechanics, Dalian University of Technology, Dalian 116024, China.
[l]International Research Center for Computational Mechanics, Dalian University of Technology, Dalian 116024, China.
[m]Center for Bio-Integrated Electronics, Northwestern University, Evanston, IL 60208, USA.
[n]College of Optoelectronic Engineering, Shenzhen University, Shenzhen, 518060, China.
[o]Bristol Composites Institute (ACCIS), University of Bristol, Bristol, BS8 1TR UK
[p]Department of Civil and Environmental Engineering, University of Missouri, Columbia, MO 65211, USA.
[q]NeuroLux, Inc., Evanston, IL 60201, USA.
[r]Department of Materials Science and Engineering, Materials Research Laboratory, University of Illinois at Urbana-Champaign, Urbana, IL 61801, USA.
[s]Department of Mechanical and Aerospace Engineering, University of Texas at Arlington, Arlington, TX 76019, USA.
[t]School of Materials Science and Engineering, Shanghai Jiao Tong University, Shanghai, 200240, China.
[u]Center for Neurobiology of Addiction, Pain, and Emotion, University of Washington, Seattle, Washington 98195, USA.
[v]Department of Pharmacology, University of Washington, Seattle, Washington 98195, USA.
[w]Simpson Querrey Institute, Northwestern University, Chicago, IL 60611, USA.
[x]Department of Biomedical Engineering, Northwestern University, Evanston, IL 60208, USA.
[y]Department of Chemistry, Northwestern University, Evanston, IL 60208, USA.
[z]Department of Neurological Surgery, Feinberg School of Medicine, Northwestern University, Chicago, IL 60611, USA.
[1]These authors contributed equally to this work.

*Corresponding authors. E-mail: jrogers@northwestern.edu; mbruchas@uw.edu; pgutruf@email.arizona.edu

This PDF file includes:

Supplementary Note 1: Materials and Methods

Supplementary Figures S1 to S12.

Supplementary Table S1 to S6.

Video S1.

References.

Supplementary Note 1: Materials and Methods

Fabrication of soft, thin microfluidic probe

Patterning photoresist (KMPR 1010, Microchem, MA, USA) on a silicon wafer followed by deep reactive ion etching (STS Pegasus ICP-DRIE; SPTS Technologies, Newport, United Kingdom) generated a silicon mold to define the geometries of the microfluidic channels. A layer of poly(methylmethacrylate) (~60 nm, PMMA A2; Microchem, MA, USA) coating applied to this wafer provided a low adhesion surface for casting of silicone elastomer polydimethylsiloxane (PDMS, 10:1 base to curing agent; Sylgard 184; Dow Corning, MI, USA). Clamping a glass slide, pre-treated with a Pt inhibitor solution (5% [3-(2-Aminoethylamino)propyl]trimethoxysilane (Sigma-Aldrich) and 95% methanol) against the PDMS (10:1 prepolymer/curing agent; Sylgard 184, Dow Corning) coated silicon mold with a layer of Scotch tape as a spacer generated a sandwich structure (1). Thermally curing the PDMS and then peeling the glass slide away yielded a thin (~80 µm) microchannel layer on the slide. Spin casting the PDMS (10:1 base to curing agent; Sylgard 184; Dow Corning, MI, USA) at 2000 rpm on a polycarbonate (PC) substrate and baking at 70 °C for 45 min generated a cover layer of PDMS with uniform thickness of 20 µm. The cover and molded microchannel layers were surface functionalized by exposure to a laboratory corona unit (Electro-Technic Products) to bond them together to complete the fabrication of the microfluidic probes. Peeling the PC substrate away and cutting with a razor blade under a microscope allowed release of the probes from the glass slide.

Fabrication of wireless control and power harvesting electronics

The fabrication began with a flexible sheet of copper clad polyimide (Cu/Polyimide/Cu, 18 µm/75 µm/18 µm; Dupont, Pyralux). Laser ablation patterned the top and bottom layers of copper into desired geometries matched to circuit requirements, including traces for the magnetic loop antenna, the leads and contact pads for the µ-ILED and the other components and the interdigitated electrodes for the reservoirs, on both sides of copper lad polyimide (ProtoLaser U4, LPKF, Germany). Electroless plating coated the interdigitated

electrodes with gold (200 nm). The electronic components, including μ-ILED (TR2227, Cree Inc.), capacitors (02016D225MAT2A, AVX Corporation; GRM0335C1H750GA01D, Murata Electronics), rectifier (SMS7621-040LF, Skyworks Solutions Inc), indicator (APG0603SURC-TT, Kingbright Company LLC), resistors (RC0201FR-075K6L, Yageo; CRCW02011K00FKED, Vishay Dale) and μ-controller (ATTINY84A-MUR, Microchip Technology) were attached to this platform using a low temperature solder (Indium Corporation). Conformal encapsulation bilayer of parylene (Specialty Coating Systems) and PDMS (dip coating) sealed the system against the biofluid penetration (2, 3). It was important to note that an epoxy (Loctite Epoxy Marine) overcoat layer was applied on critical electronic components to prevent their delamination from contact pads during in vivo studies.

Preparation of flexible membrane

Polystyrene-block-polybutadiene-block-polystyrene (SBS, Sigma-Aldrich, MO, USA) was dissolved in toluene (4 g/40 ml) and then casted on a mold release spray (Ease Release 200, Mann Release Technologies, Inc., PA, USA) treated silicon wafer. The SBS films were then cured at 60 °C (~3 hours) and then 95 °C (overnight). Sputtering deposition (AJA International) a bilayer of Ti/SiO$_2$ (5 nm/20 nm) rendered the surface of the SBS film hydrophilic to facilitate the loading of aqueous drugs.

Assembly and test

A mechanically milled block of cyclic olefin copolymer (COC; thickness: 1 mm) served as the platform for the micropump chamber and drug reservoirs. Coating the surfaces of these reservoirs with Ti/SiO$_2$ by sputtering (5 nm/50 nm, AJA International) yielded hydrophilic surfaces. **Figure S12** shows schematic illustrations of the assembly process. Cylindrical features of micropump chambers aligned on the interdigitated electrodes of the flexible PCB platform and bonded with commercially available sealant (3M marine adhesive sealant fast cure 5200) formed sealed micropump chambers for each of the reservoirs. Flexible membranes of SBS (~150 μm) created in the manner described above provided impermeable barriers bonded on the bottom of hemispherical drug reservoirs with a commercially available pressure

sensitive adhesive (Adhesive Research, Inc. EL-8932EE). The hemispherical drug reservoirs with bonded flexible membrane were aligned and bonded to the micropump chamber using the same sealant. Next, the outlets of the hemispherical drug reservoirs were aligned and bonded with the inlets of the microfluidic channels using same pressure sensitive adhesive. Bonding of the μ-ILED probe onto the microfluidic probe using a silicone adhesive (KWIK-SIL, World Precision Instruments) finished the assembly of the device. The injectable optofluidic probe of finished device was bent for implantation in *in vivo* studies.

Power characterization

Power characterization was performed in a 25×25 cm CPP cage and 15×33 cm home cage with input power of 6 or 3 W. Voltage and power measurements were conducted with decreasing load in the center of the 15×33 cm cage. Maximum power was achieved with a 6.8 kΩ shunt resistor, and subsequent measurements utilized this load. Voltage and power were measured at increasing angles by rotating the device on a custom-made nonmetallic measurement utility. Voltage measurements were taken with a battery powered multimeter (Aneng AN8008) to avoid noise induced by the RF field and ground loops. A voltage regulator can be used in order to regulate system voltage and ensure constant power output of the implant (**Figure S3F**). Voltage was spatially mapped using the previously mentioned load and 6 or 3 W input power. Power consumption of the implant for different pulsing states was measured with a 3.3 V input voltage and μ-ILED pulses of 30 Hz. Average power was obtained by integration of power over time.

Theoretical modelling of drug diffusion

An analytical model of drug diffusion into the brain tissue following infusion is established. The brain tissue has an extracellular space fraction α, which is defined as the volume ratio of the extracellular phase to the entire brain tissue (4). The injected drug is initially distributed uniformly through a sphere of radius r_0 in the brain tissue, with the initial concentration C_0, and spreads within the extracellular space in a radial pattern such that the diffusion is governed by the following equation in a spherically symmetric coordinate system:

$$D\left(\frac{\partial^2 C}{\partial r^2} + \frac{2}{r}\frac{\partial C}{\partial r}\right) = \frac{\partial C}{\partial t} \quad (r \geq 0),$$ (Eq S1)

where D is the apparent diffusion coefficient of the drug in the brain tissue, and C the drug concentration, depending on time t and spatial coordinate r that represents the distance from the origin.

Introducing $u = Cr$, Eq S1 is transformed into

$$D\frac{\partial^2 u}{\partial r^2} = \frac{\partial u}{\partial t} \quad (r \geq 0),$$ (Eq S2)

with the initial condition

$$u\big|_{t=0} = \begin{cases} C_0 r & (0 \leq r \leq r_0) \\ 0 & (r > r_0) \end{cases}$$ (Eq S3)

and the boundary conditions

$$u\big|_{r=0} = u\big|_{r=\infty} = \frac{\partial u}{\partial r}\bigg|_{r=\infty} = 0.$$ (Eq S4)

The Fourier sine transform with respect to r, together with the boundary conditions of Eq S4, gives an ordinary differential equation with respect to t, whose solution, satisfying the initial condition in Eq S3, is obtained analytically. The inverse Fourier sine transform gives the analytical solution of u, which in turn yields the distribution of drug concentration:

$$C = \frac{C_0}{2}\left\{\text{erf}\frac{r+r_0}{2\sqrt{Dt}} - \text{erf}\frac{r-r_0}{2\sqrt{Dt}} + \frac{2}{r}\sqrt{\frac{Dt}{\pi}}\left\{\exp\left[-\frac{(r+r_0)^2}{4Dt}\right] - \exp\left[-\frac{(r-r_0)^2}{4Dt}\right]\right\}\right\}.$$ (Eq S5)

Here, the initial radius r_0 of the injected drug distributed in the brain tissue is determined by equality of injected volume and that within the extracellular space, giving $r_0 = \left[3U/(4\pi\alpha)\right]^{1/3}$, where U is the injected volume.

Monte Carlo simulations on brain tissue

Optical simulations were performed using the Monte Carlo stochastic photon propagation method in brain tissue. The simulation volume is comprised of 300^3 bins, each with $(8 \mu m)^3$ volume. A total of 4.6×10^6 photons were launched into the numerical volume. The blue μ-LED's footprint is 0.22×0.27 mm^2 and has 120º full divergence angle. The brain tissue parameters are: $\mu_a = 1.2$ cm^{-1}, $\mu_s = 211$ cm^{-1} and g = 0.85 (5, 6). The photon irradiance was normalized with respect to the reference input power to provide different illumination scenarios, from 0.25 to 2.0 mW as seen in Fig. S6. For each of these input powers the illumination volume was calculated at three different irradiance thresholds, 0.1, 1.0 and 10 mW/mm^2 (see Table S3)

Flow rate measurement

Flow rate measurements used an aqueous fluorescent particle suspension (1 wt%, FluoSpheres™ carboxylate-modified microspheres, 1.0 µm, yellow-green fluorescent (505/515)) injected into the reservoirs. A function generator provided electrical current to the interdigitated electrodes at a voltage of 3V, pulsed at 490 Hz with different duty cycles (30% - 90%). The tip of the microfluidic channels was implanted into a brain phantom to simulate *in vivo* environment. The delivery process was captured and recorded with a microscope system equipped with a high speed camera. PIV and PTV analyses yielded velocities of flow in the channel using the PIV interrogation algorithm developed by Liao and Cowen (7). This algorithm implements an FFT-based continuous sub-window shifting approach to achieve sub-pixel accuracy, and is executed in MATLAB environments. Due to the relatively long exposure time, motion blur of the particles was observed in images. To reduce PIV and PTV error caused by the motion blur, we applied a Gaussian low-pass filter to smooth the images before the PIV and PTV analysis. We note the field of view (FOV) of the images is only about two to three times of the distance of the particle movement during the time interval of two consecutive images. Hence, the size of PIV interrogation windows was set to be sufficient large (i.e., 120×40 pixels) to ensure successful PIV tracking. We also excluded tracking

results with correlation coefficients less than 0.75. The results using PIV and PTV tracking methods were generally consistent.

Flow rate modelling

Eq 1 in the main text typically overestimates the flow rate as it does not account for flow resistance in microfluidic channel and the stiffness of the flexible membrane. The analytical model developed in (2) was used here to better predict the flow rate for various given applied effective current i. The model is based on the rate form of ideal gas law of the micropump chamber:

$$\dot{P}(V + V_0) + P\dot{V} = \dot{n}RT, \tag{Eq S6}$$

where P is the pressure, V_0 and V are the initial volume and volume change of air inside the micropump chamber, respectively, n is the number of moles of air, R is the ideal gas constant, and T is the temperature. The gas generation rate $\dot{n}$ can be related to the effective current i by,

$$\dot{n} = \frac{3i}{4F}, \tag{Eq S7}$$

and F is the Faraday's constant. It is worth noting here that volume increase V in the micropump chamber is just the volume of drug delivered such that $\dot{V}$ is the flow rate Q.

The pressure difference between the micropump chamber and atmosphere pressure $P - P_0$ is obtained by accounting for (1) the flow resistance in microfluidic channel, and (2) the resistance from the stiffness of the flexible membrane, as

$$P - P_0 = \frac{32\mu L\dot{V}}{w^4} + f(V), \tag{Eq S8}$$

where w and L are the width (the height is the same as the width) and length of the delivery channel, and μ is the viscosity of the drug. Function $f(V)$ that quantifies the pressure difference due to the volume increase V, was obtained from finite element analysis.

Combining Eq S6 and Eq S8, the differential equation of the system is given by

$$\left[\frac{32\mu L}{w^4}\ddot{V} + f'(V)\dot{V}\right](V + V_0) + \left[\frac{32\mu L}{w^4}\dot{V} + f(V) + P_0\right]\dot{V} = \dot{n}RT,$$

<div align="right">(Eq S9)</div>

The numerical solution to the above under initial conditions $V(t = 0) = 0$, and $\dot{V}(t = 0) = 0$ gives the flow rate $Q = \dot{V}$ over time shown in **Figures 2K and L**.

Experimental animals

Wild-type C57BL/6J, C57BL/6NHsd and vGAT-cre male and female mice were used in this study. Mice were 6-10 weeks old at the time of test, weighing 20-33 g each, given access to food pellets and water ad libitum, and maintained on a 12 hr: 12 hr light: dark cycle (lights on at 7:00 AM). All mice were kept in a sound-attenuated, isolated holding facility in the lab one week prior to surgery, post-surgery, and throughout the duration of the behavioral assays to minimize stress. Strains with specific genetic modifications (vGAT-cre) and wild-type littermate control animals were bred from heterozygous parents as well. All procedures were approved by the Animal Care and Use committee of Washington University and Northwestern University and conformed to US National Institutes of Health guidelines.

Surgery

After the mice were acclimated to the holding facility for at least seven days, the mice were anaesthetized in an induction chamber (4% isoflurane) and placed into a stereotaxic frame (Kopf Instruments, Model 1900) where they were maintained at 1-2% isoflurane. Mice used for optogenetic experiments then received a unilateral infusion of the channelrhodopsin virus via blunt needle (86200, Hamilton Com) at a rate of 0.1 μL/min (RTPT: AAV5-EF1α-DIO-hCHR2-(H134R)-eYFP, 0.4 μL, VTA: AP -3.15, ML ±0.5, DV -4.25 ; Locomotion: pAAV.CAG.hChR2(H134R)-mCherry.WPRE.SV40, 0.5μL, dorsal HIPP: AP:-1.8, ML: -1.00, DV: -2.0). To ensure that the implanted devices adhered to the skull, circular grooves were drilled into the top of the skull. These grooves provided extra surface area for the super glue that fixed the devices to the skull to adhere to, creating a strong, but lightweight bond. Mice were allowed to recover for about a week before contraversive rotation experiments, and 3 weeks for optogenetic

experiments to permit optimal expression of the virus. For optogenetic experiments, mice were generally not implanted until one week prior to behavioral testing, though in some cases were tested sooner as described below (VTA: AP -3.15, ML ±0.5, DV-4.25; DH: AP:-1.8, ML: - 1.00, DV: -2.0). For the immuno-glial response experiment, optofluidic devices and double 26 gauge guide cannulas (Plastics One, Inc.) were implanted into the dorsal hippocampus (stereotaxic coordinates from bregma (mm): optofluidic device: AP:-1.8, ML: -1.0, DV: -2.0; cannula: AP:-1.8, ML: ±1.0, DV: -2.0).

Immunohistochemistry

Immunohistochemistry was performed as described previously (8, 9). Briefly, mice were anesthetized with Avertin (1ml) transcardially perfused with cold 4% paraformaldehyde (PFA) in phosphate buffer. Brains were removed, post fixed in PFA for 24 h, and then immersed in 20%, and 30% sucrose in phosphate buffer for 24 h each. Transverse sections (50 µm) were washed three times in PBS and blocked in PBS containing 0.5% Triton X-100 and 5 % normal horse serum. Sections were then incubated for ~16 hr at 4 ℃ temperature in mouse anti-GFAP (Pharmagene Labs, Colorado Springs, CO), goat anti-Iba1 (Abcam Inc. Toronto, ON). Following incubation, sections were washed three times in PBS and then incubated for 2 hr at room temperature in Alexa Fluor® 594 AffiniPure Donkey Anti-Mouse IgG (H+L) and Alexa Fluor® 647 AffiniPure Donkey Anti-Goat IgG (H+L) (Jackson Immuno Research Laboratories, Inc. West Grove, PA), then washed three times in PBS, coverslipped with DAPI- mounting media (Sigma, St. Louis, MO). All sections were imaged on both fluorescence microscopes and confocal microscopes. Gain and exposure time were constant throughout each experiment.

Immuno-glial response in implanted tissues

C57BL/6NHsd mice (n=6) were implanted with optofluidic devices into the dorsal hippocampus and allowed to recover for one week before perfusion. Immunohistochemistry was performed as described previously (9).

Behavioral experiments

Pharmacologically induced contralateral rotations: Wireless optofluidic devices were implanted into the ventral tegmental area (VTA) of wild-type (C57BL/6J) mice. Seven days after implantation, we loaded 1 drug chamber with either [D-Ala^2, N-MePhe^4, Gly-ol^5]-enkephalin (DAMGO, 200 pmol, Tocris) or artificial cerebral spinal fluid (ACSF) as a vehicle control. To deliver the drug, mice were gently placed into a NFC wired home cage, at which point fluidic delivery was signaled. Mice were able to freely walk around during the infusion and diffusion period (~4 min). Mice were then placed into an open field chamber (50 × 50 cm) and allowed to explore for 1 hour. At the end of the hour, mice were placed back into the home cage. 24 hours later, mice went through the same infusion protocol, but received the secondary delivery. DAMGO and ACSF test days were counterbalanced across mice. Importantly, the same drug reservoir was used to demonstrate the reusability of the reservoirs. General locomotor activity was automatically recorded and calculated by Ethovision (Noldus). Contraversive rotations were scored offline by a blind observer. A mouse was considered to have completed a full rotation if it completed a 360° turn in under 10 seconds. This conservative quantification was used to avoid mistaking rotations for general turning behavior (e.g., 90° or 180°).

Real-Time Place Test: We used custom-made unbiased, balanced two-compartment conditioning apparatus (52.5 × 25.5 × 25.5 cm) as described previously (10, 11). vGAT-cre mice were allowed to freely roam the entire apparatus for 20 min. Entry into one compartment triggered constant photostimulation 10Hz, (473 nm, 10 ms pulse width) while the mouse remained in the light paired chamber. Entry into the other chamber ended the photostimulation. The side paired with photostimulation was counterbalanced across mice. Time spent in each chamber and total distance traveled for the entire 20-minute trial were measured using Ethovision 10 (Noldus Information Technologies, Leesburg, VA).

Locomotor activity: C57BL/6NHsd mice were allowed to recover from implantation for 3 days prior to optofluidic behavioral testing. On test days, animals were placed in a cage with the same dimensions as their home cage, which was equipped with the near-field antenna. Locomotion was tracked by a VideoMot2 Video Tracking system (TSE). On day 1, mice received no drug infusion and were able to freely explore

the chamber for 2 minutes. On day 2, animals were split into 2 groups (APV and non-APV) and placed into the same home cage. During the first minute, all animals were allowed to freely explore the chamber without optical stimulation. During the second minute, all mice received optical stimulation. For the APV group, APV (10 μg/μL in ACSF, 0.25 μg/ side, Sigma, St. Louis, MO) was wirelessly delivered into DH 15 min before behavioral testing on day two. For mice tested on the detrimental effects of device implantation on locomotion, mice were tested 1 day, 3 days, or 30 days after implantation.

Fig. S1. Weight and complete hardware system of injectable optofluidic system. Weight of a conventional metal cannula *(A)* and a wireless, injectable optofluidic system *(B)*. *(C)* Picture of the external hardware. *(D)* Screen image from a custom software application as a user interface.
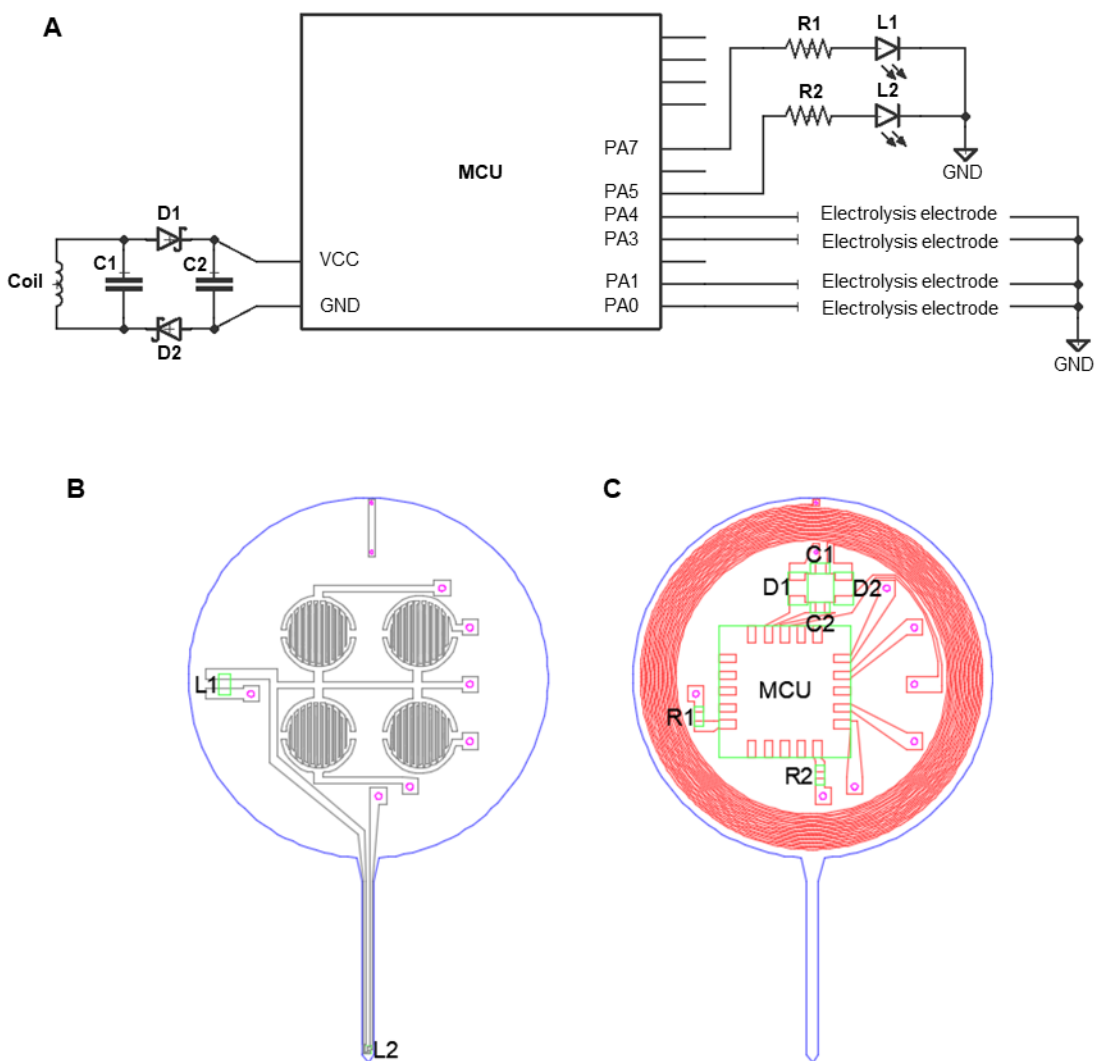
Fig. S2. Circuit designs of injectable optofluidic system. (*A*) Circuit diagram. (*B-C*) Interdigitated electrodes and wireless electronics design.
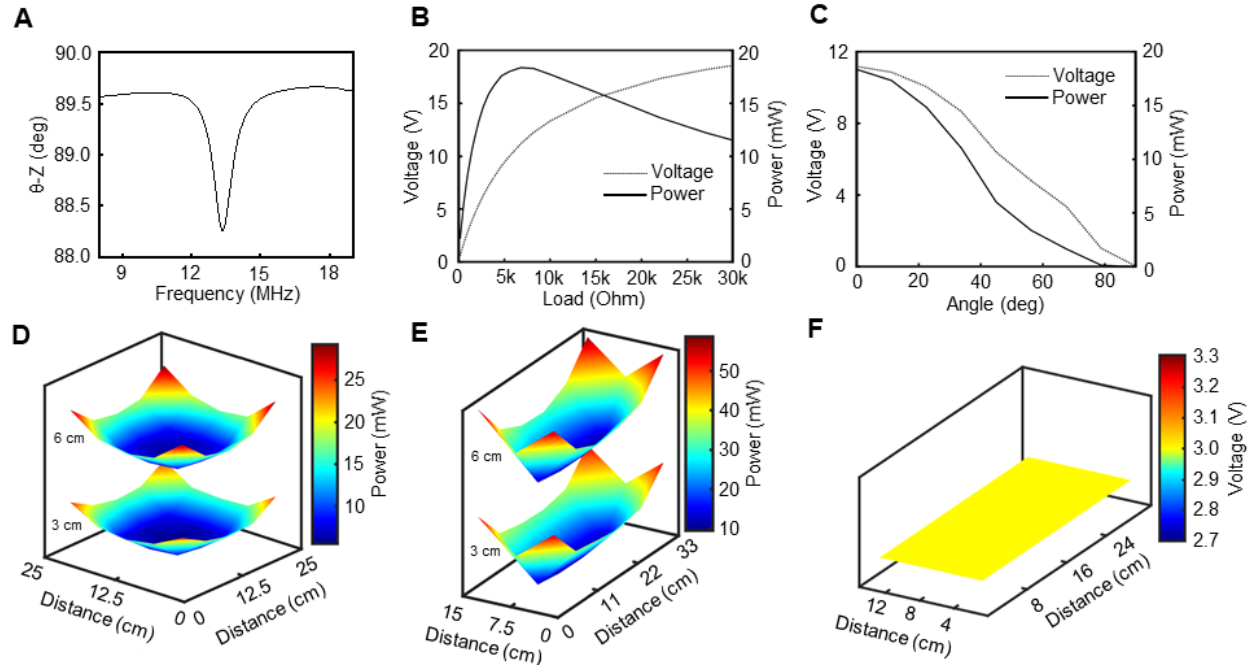
Fig. S3 Electrical Characterization. *(A)* Phase response of the receiver antenna, highlighting the resonant frequency at ~13.56 MHz. (*B*) Measurement of rectifier voltage and power with increasing load positioned in the center of a field created by a 25 cm × 25 cm cage with 6W primary antenna power. (*C*) Measurement of voltage and power with a 6.8 kΩ load, at a height of 3 cm above ground with increasing angle. (*D*) Rectified power at the implant measured in a 25 cm × 25 cm CPP cage with a 3 W input power at implant heights of 3 and 6 cm above ground. (*E*) Rectified power at the implant measured in a 15 cm × 33 cm home cage with a 3 W input power at implant heights of 3 and 6 cm above ground. (F) Regulated voltage with applied load in a home cage.
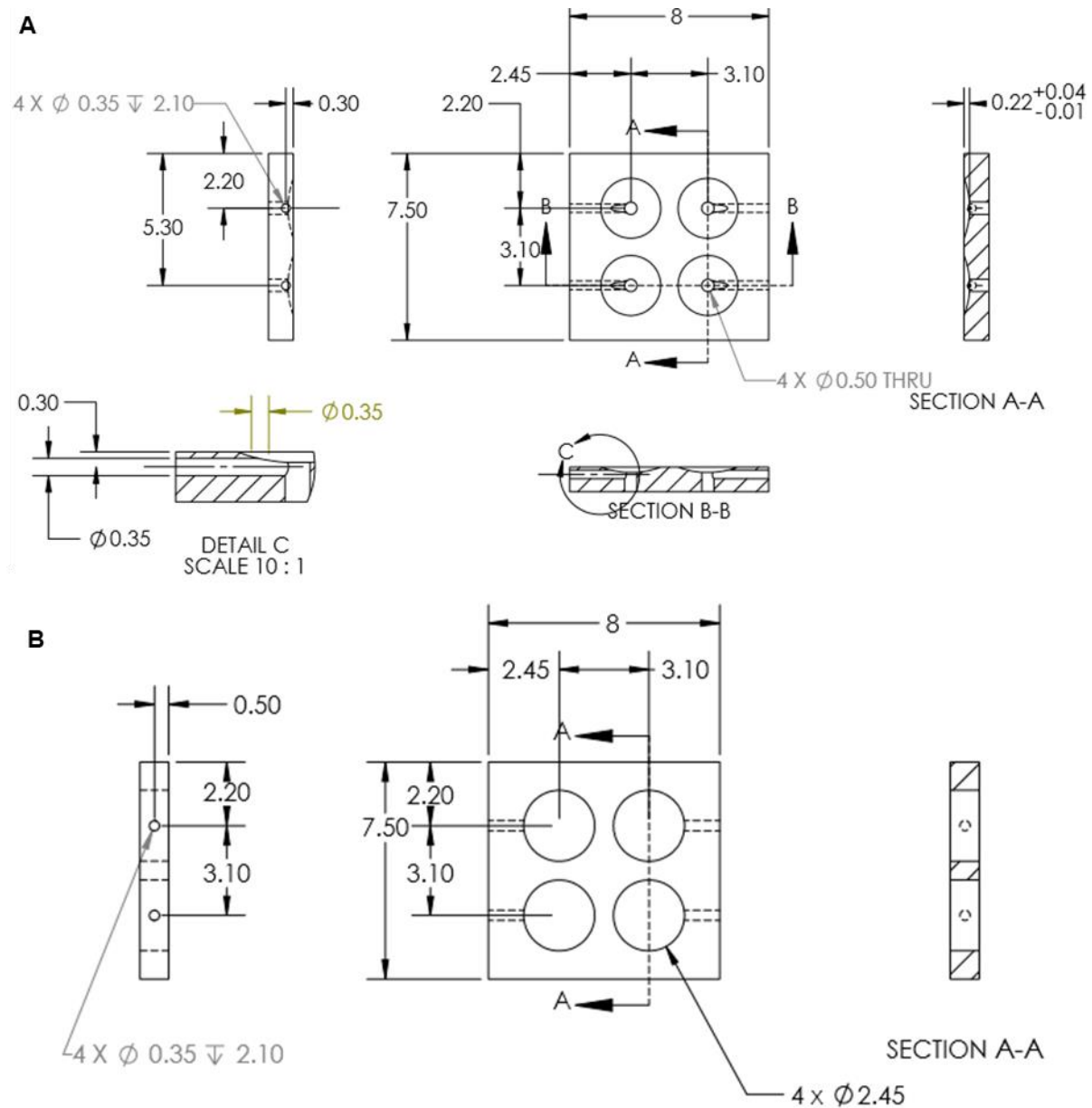
Fig. S4 Technical drawing with dimensions for drug reservoirs and micropump chambers.

(*A*) Drug reservoirs. (*B*) Micropump chambers.
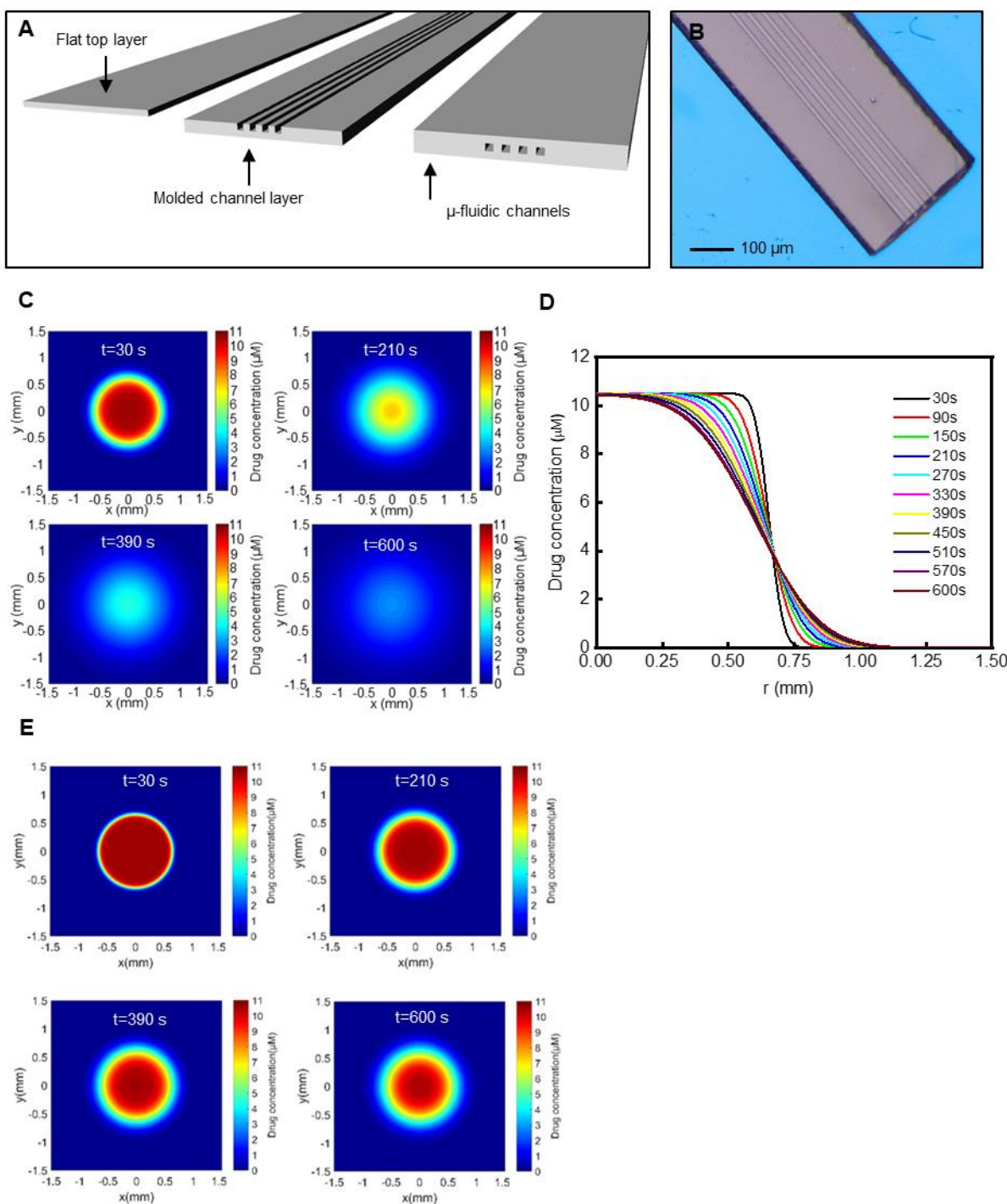
Fig. S5 Preparation and drug diffusion of soft microfluidic probe. *(A)* Schematic diagram of the bonding process and *(B)* optical micrograph of soft microfluidic probe for programmable pharmacology. (*C*) Contours of drug concentration for t = 30, 210, 390, and 600 s with the diffusion

of small molecule. (*D-E*) Distribution of drug concentration along radial direction for t = 30, 90, 150, 210, 270, 330, 390, 450, 510, 570, and 600 s, and contours of drug concentration for t = 30, 210, 390, and 600 s with the diffusion of macromolecule into brain.
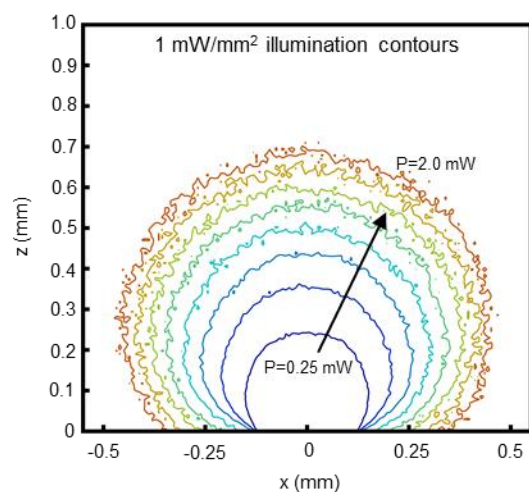
Fig. S6. Illumination contours that represent the 1 mW/mm² illumination threshold when illuminated at different optical input powers ranging from 0.25 to 2 mW.
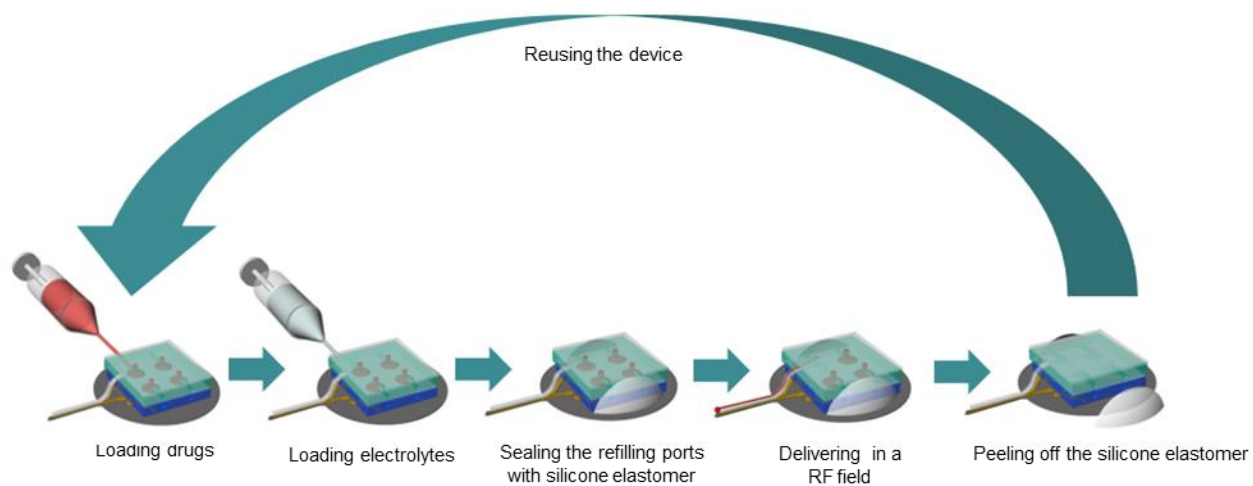
Fig. S7. Schematic illustration of the steps for loading the drug reservoirs and micropump chambers, sealing of the refilling ports, and reusing the device.
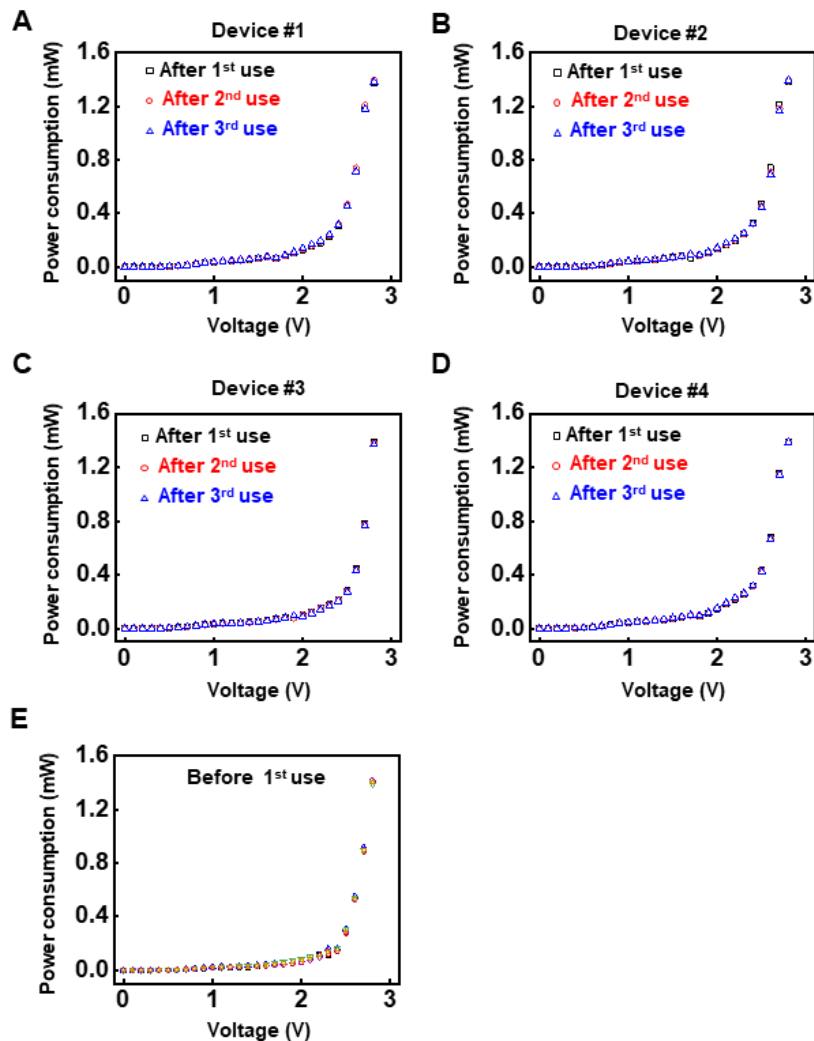
Fig. S8. Power consumption-voltage characteristics of electrochemical micropumps. (A-D) Power consumption-voltage characteristics of four electrochemical micropumps after the first, second, and third use. Each micropump was used three times. (E) Power consumption-voltage characteristics of six devices before the first use. The applied voltage to the Au electrodes were set from 0 to 2.8 V and 50 mM NaOH solution was used to increase the conductivity of water.
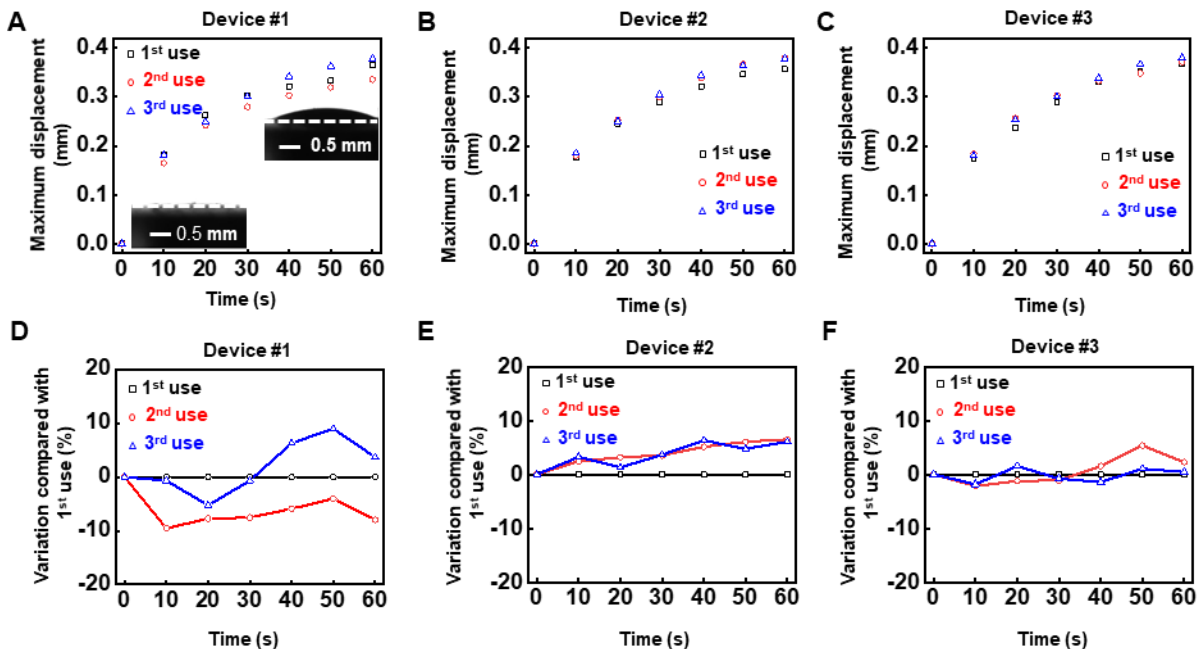
Fig. S9. The maximum displacement of flexible membrane during the first, second, and third uses. *(A)-(C)* Time-dependent maximum displacement of flexible membrane induced by water electrolysis. Black rectangular, red circle, and blue triangle represent the data during the first, second, and third use, respectively. Inset: (left bottom) membrane displacement at $t = 0$; (right upper): membrane displacement at $t = 60$ s. Voltage was set at 2.8 V. 50 mM NaOH was used. *(D)-(F)* Variation of the maximum membrane displacement compared with the first use. Variation (%) here is defined as $(D_n-D1)/D1 \times 100$ ($n=2$ for second use; $n=3$ for third use); D represents maximum membrane displacement. The calculation is based on data in *(A), (B), and (C),* respectively.
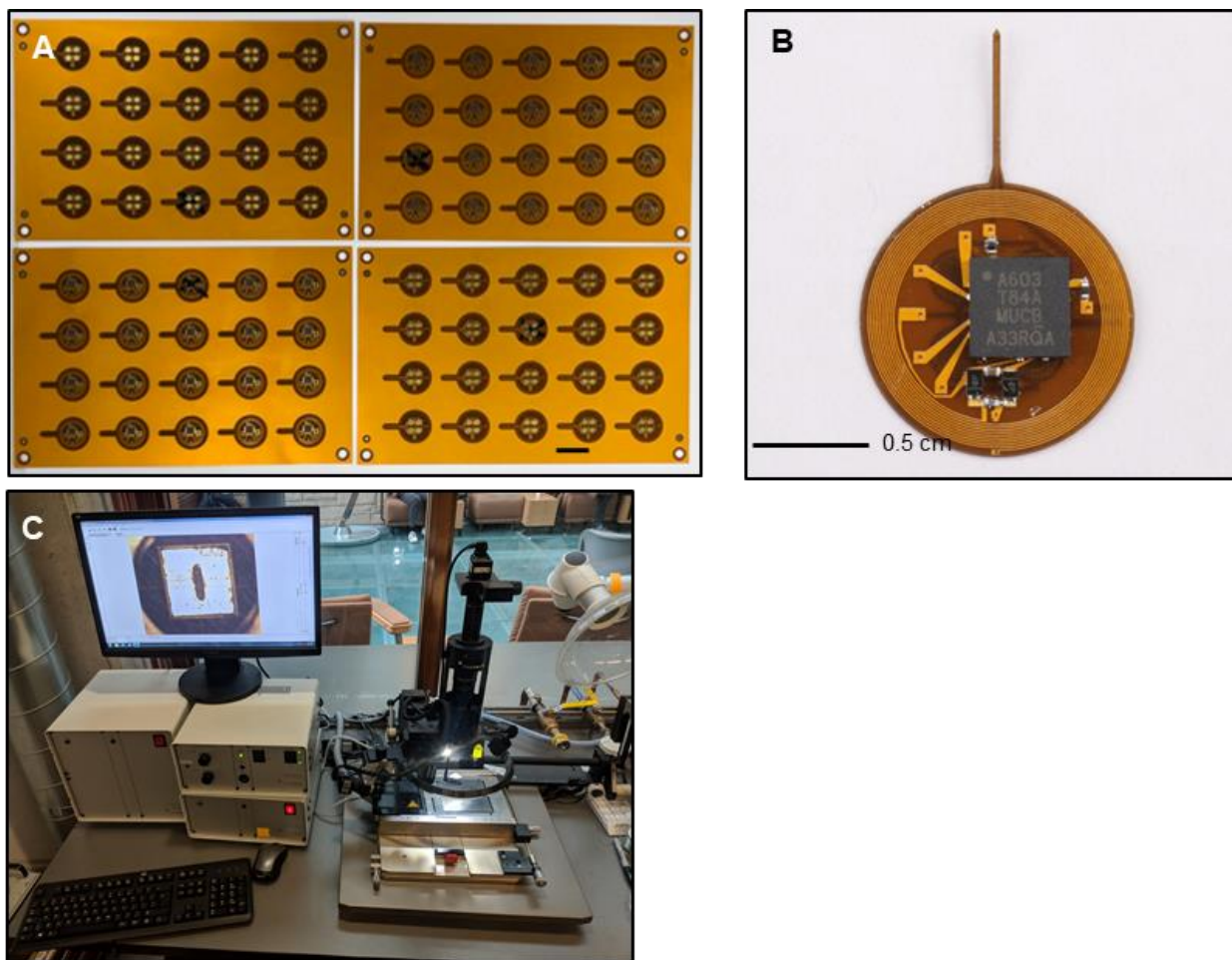
Fig. S10. Manufacturing of electronics using flexible printed circuit board technology. (A) Picture of panels from an exploratory manufacturing run; each supports 20 devices. Scale bar: 1 cm. (B) Picture of a device with mounted electronic components, including μ-ILED, capacitor, rectifier, and μ-controller. (C) Photographic image of a pick-and-place machine to mount the electronic components.
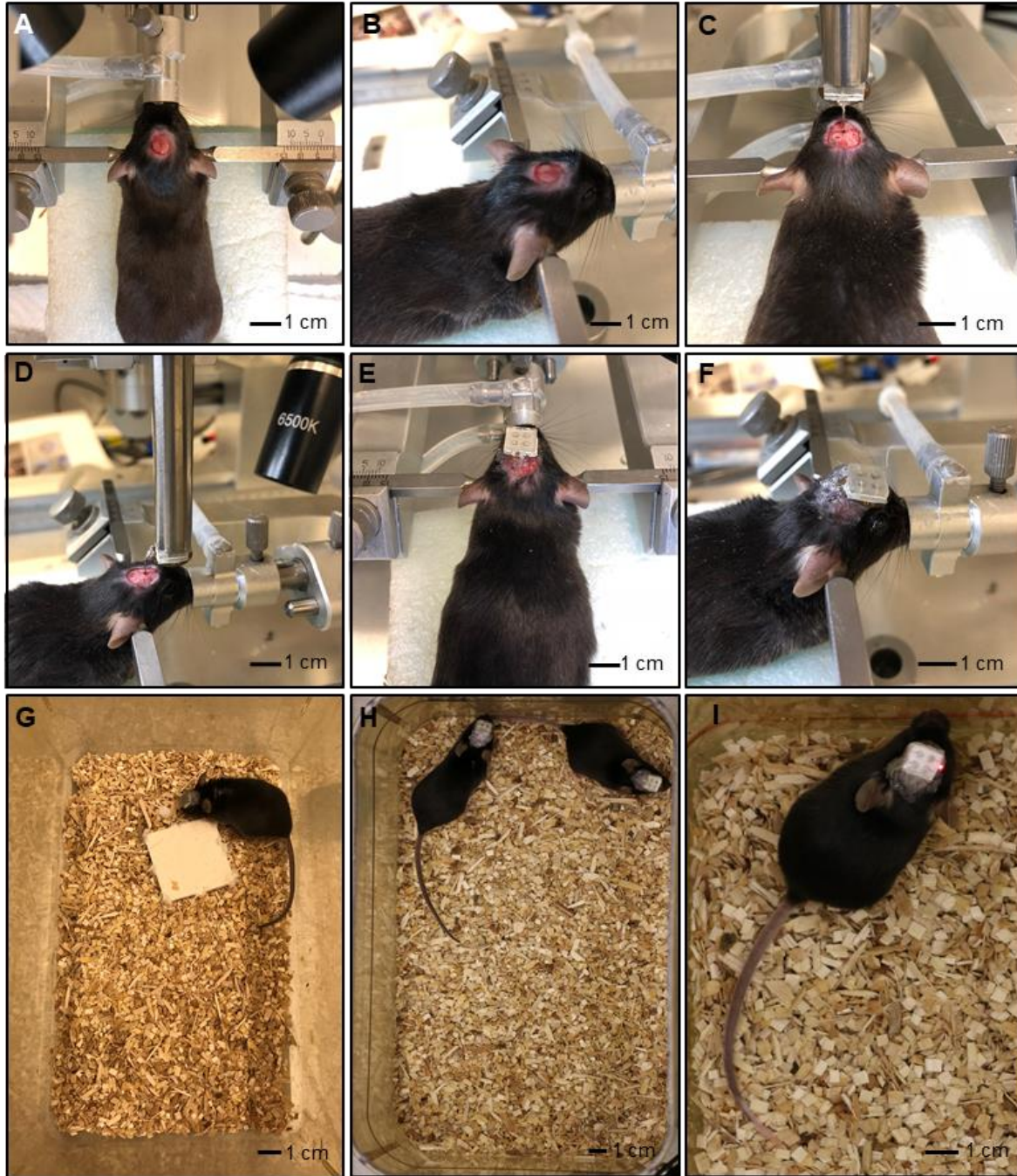
Fig. S11. Illustration of surgical procedures for implanting the device in the dorsal hippocampus and recovered mouse. *(A–F)* Images of the surgical steps for *(A, B)* holding and *(C)* positioning the body of the device, *(D)* injecting the needle into the deep brain, and *(E, F)* gluing the device on the skull, respectively. *(G-H)* Images of recovered mice after *(G)* 3 days *(H)* 4 weeks from surgery. *(I)* Images of the operating of devices in the home cage.

Apply sealant on the micropump chambers → **Attach micropump chambers on the electronic station** → **Attach flexible membrane on the drug reservoirs with adhesive** → **Apply sealant and attach drug reservoirs on the top of micropump chambers**

Bend the probes for implantation ← **Bond μ-LED with μ-fluidic probes** ← **Attach microfluidic channels on the top of drug reservoirs**
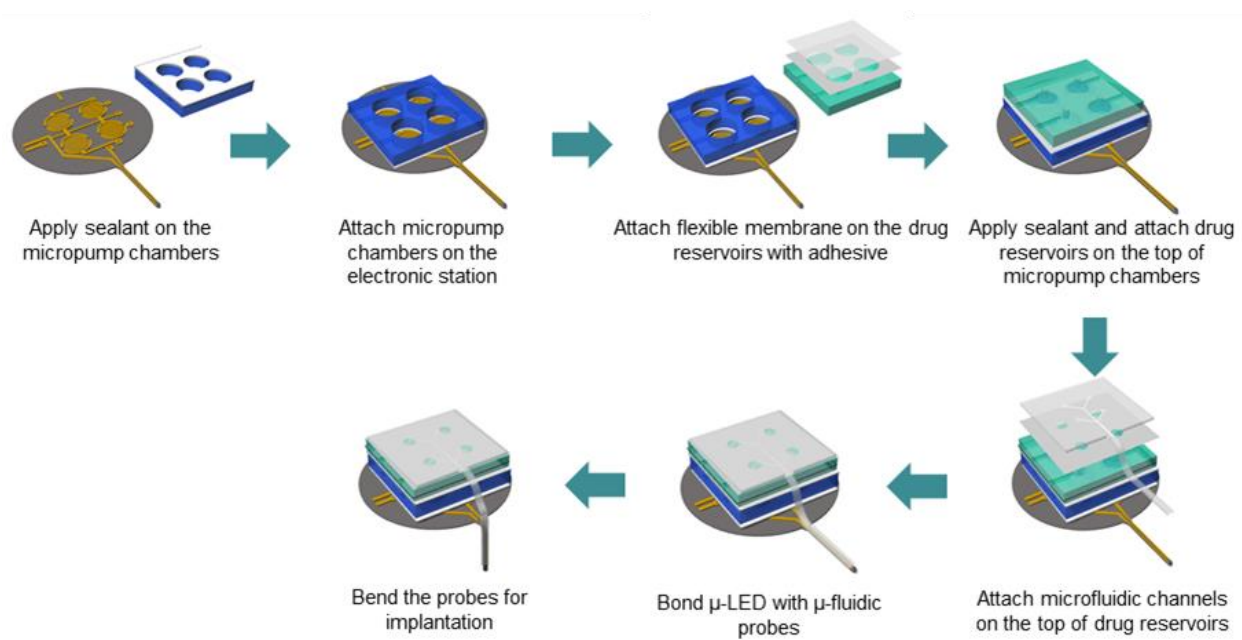
Fig. S12. Schematic illustrations of the steps for assembly of the device.

Table S1. Information on chip components of wireless injectable microsystem.

	Components	Product #	Manufacturer
MCU	Microcontroller Unit, 4mm x 4mm x 0.75mm	ATtiny84A-MUR	Microchip Technology
L1	Indicating LED, 631nm, 0.65mm x 0.35mm x 0.25mm	APG0603SURC-TT	Kingbright
L2	Stimulating LED, 465nm, 220um x 270um x 50um	C460TR2227-0216	Cree Inc.
C1	Capacitor, 75pF, 0.6mm x 0.3mm x 0.33mm	GRM0335C1H750GA01D	Murata Electronics
C2	Capacitor, 2.2uF, 0.6mm x 0.3mm x 0.4mm	02016D225MAT2A	AVX Corporation
D1, D2	Schottky Diode, 1mm x 0.6mm x 0.5mm	SMS7621-040LF	Skyworks Solutions Inc.
R1	Resistor, 5.6kOhm, 0.6mm x 0.3mm x 0.26mm	RC0201FR-075K6L	Yageo
R2	Resistor, 1kOhm, 0.6mm x 0.3mm x 0.28mm	CRCW02011K00FKED	Vishay Dale

Table S2. Summary of previous studies that quantified the "functional" spread of a drug by measuring changes in Fos activity.

Publications	Year	Drug/Volume	Radius/Volume
Faure et al., Journal of Neuroscience	2008	DNQX/0.5μL	0.978mm/3.92mm^3
Faure et al., PLoS One	2010	Muscimol/0.5μL	0.304mm/0.11mm^3
Richard et al., Journal of Neuroscience	2011	DNQX/0.5μL	0.38mm/0.23mm^3
Castro et al., Neuropsychopharmacology	2016	Scopolamine/0.5μL	0.23mm/0.051mm^3

Table S3. Effective illumination volume for different optical input power and illumination thresholds.

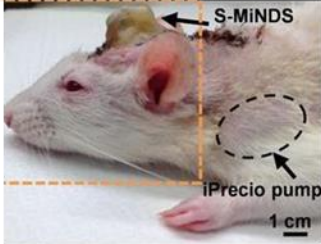| P (mW)	I (mW/mm²)	Illuminated volume (mm³)		
		@ 10 mW/mm²	@ 1 mW/mm²	@ 0.1 mW/mm²
0.25	4.21	0	12.45×10^{-3}	0.457
0.50	8.41	0	32.98×10^{-3}	1.332
0.75	12.63	1.64×10^{-3}	61.15×10^{-3}	2.329
1.00	16.83	3.35×10^{-3}	97.30×10^{-3}	3.358
1.25	21.04	4.85×10^{-3}	141.93×10^{-3}	4.377
1.50	25.25	6.24×10^{-3}	193.62×10^{-3}	5.379
1.75	29.46	7.66×10^{-3}	251.60×10^{-3}	6.353
2.00	33.67	9.20×10^{-3}	315.61×10^{-3}	7.297

Table S4. Percent error analysis between experiment and modeling of maximum flow rates at various applied currents.

Applied current(mA)	Flow rate_E (μL/min)	Flow rate_M (μL/min)	Percent Error (%)
0.2	0.88	0.89	1.14
0.28	1.21	1.21	0
0.26	0.91	1.13	24.18
0.42	1.09	1.73	58.72
0.43	1.50	1.77	18.00
0.42	1.12	1.73	54.46
0.48	1.45	1.94	33.80
0.45	1.28	1.84	43.75
0.47	1.26	1.91	51.59
0.55	1.66	2.18	31.33
0.56	1.79	2.21	23.46

Table S5. The relationship between applied current and time required to reach maximum flow rate or total time to deliver > 80% of fluid housed in the reservoir.

Applied current (mA)	Time to maximum flow rate (s)	Time to deliver >80% of fluid housed in the reservoir (s)
0.06	35.91	97.87
0.12	22.01	50.71
0.18	17.19	35.01
0.24	14.49	27.17
0.30	12.99	22.47
0.36	11.88	19.33
0.42	11.06	17.09
0.48	10.43	15.39
0.54	9.91	14.06
0.60	9.53	12.99

Table S6. Summary of recent available wireless fluidic devices. List of features for the battery-free injectable microsystem (this device), miniaturized neural drug delivery system (Dagdeviren et al., 2018 Sci. Transl. Med.), and battery-powered optofluidic device (Jeong et al., 2015 Cell), with details and comparative assessment.

	Jeong et al., 2015 *Cell*	Dagdeviren et al., 2018 *Sci. Transl. Med.*	Zhang and Castro et al. (this device)
Capabilities	Fluid delivery and optogenetics	Fluid delivery and electroencephalogram	Fluid delivery and optogenetics
Weight	1.855g	>6.6g	0.29g
Dimensions	15 x 15 x 7mm^3	> 14.4 x 15 x 24.8mm^3	π x 5^2 x 4mm^3
Power Source	Battery	Battery	Near Field Communication
Power Consumption	>100mW	-	1-3mW
Pump	Thermal	iPrecio SMP-300	Electrochemical
# of Reservoirs	Four	Two	Four
Reservoirs Use	Single Use	Refillable	Refillable
Lifetime	Limited Operation	~2 months	Unlimited
Representative Image			

Video S1. Mice implanted with the device show normal behaviors. Two mice implanted with the device show normal locomotor (e.g., rearing, walking, exploring) and social (e.g., sniffing, climbing) behaviors.

References

1. McCall JG*, et al.* (2017) Preparation and implementation of optofluidic neural probes for in vivo wireless pharmacology and optogenetics. *Nat Protoc* 12(2):219-237.
2. Zhang Y, et al. (2019) Battery-free, fully implantable optofluidic cuff system for wireless optogenetic and pharmacological neuromodulation of peripheral nerves. Science Advances 5(7):eaaw5296.
3. Shin G, et al. (2017) Flexible Near-Field Wireless Optoelectronics as Subdermal Implants for Broad Applications in Optogenetics. Neuron 93(3):509-521.
4. Nicholson CJBr (1985) Diffusion from an injected volume of a substance in brain tissue with arbitrary volume fraction and tortuosity. *Brain Res* 333(2):325-329.
5. Yaroslavsky AN*, et al.* (2002) Optical properties of selected native and coagulated human brain tissues in vitro in the visible and near infrared spectral range. *Phys Med Biol* 47(12):2059-2073.
6. Jacques SL (2013) Optical properties of biological tissues: a review. *Phys Med Biol* 58(11):R37-R61.
7. Liao Q & Cowen EA (2005) An efficient anti-aliasing spectral continuous window shifting technique for PIV. *Exp Fluids* 38(2):197-208.
8. Corcoran KA, Leaderbrand K, & Radulovic JJJoN (2013) Extinction of remotely acquired fear depends on an inhibitory NR2B/PKA pathway in the retrosplenial cortex. *J Neurosci* 33(50):19492-19498.
9. Jeong JW, et al. (2015) Wireless Optofluidic Systems for Programmable In Vivo Pharmacology and Optogenetics. Cell 162(3):662-674.
10. Stamatakis AM & Stuber GDJNn (2012) Activation of lateral habenula inputs to the ventral midbrain promotes behavioral avoidance. *Nat Neurosci* 15(8):1105.
11. Jennings JH*, et al.* (2013) Distinct extended amygdala circuits for divergent motivational states. *Nature* 496(7444):224.